

The Bigger the Better? Accurate Molecular Potential Energy Surfaces from Minimalist Neural Networks

Silvan Käser,[†] Debasish Koner,[‡] and Markus Meuwly^{*,†}

[†]*Department of Chemistry, University of Basel, Klingelbergstrasse 80, CH-4056 Basel,
Switzerland.*

[‡]*Department of Chemistry, Indian Institute of Technology Hyderabad, Kandi,
Sangareddy-502285, Telangana, India*

E-mail: m.meuwly@unibas.ch

November 28, 2024

Abstract

Atomistic simulations are a powerful tool for studying the dynamics of molecules, proteins, and materials on wide time and length scales. Their reliability and predictiveness, however, depend directly on the accuracy of the underlying potential energy surface (PES). Guided by the principle of parsimony this work introduces KerNN, a combined kernel/neural network-based approach to represent molecular PESs. Compared to state-of-the-art neural network PESs the number of learnable parameters of KerNN is significantly reduced. This speeds up training and evaluation times by several orders of magnitude while retaining high prediction accuracy. Importantly, using kernels as the features also improves the extrapolation capabilities of KerNN far beyond the coverage provided by the training data which solves a general problem of NN-based PESs. KerNN applied to spectroscopy and reaction dynamics shows excellent performance on test set statistics and observables including vibrational bands computed from classical and quantum simulations.

Molecular dynamics (MD) simulations have long been a cornerstone of research in fields ranging from chemistry and biology to materials science and drug discovery.¹⁻³ Such simulations offer a unique lens through which the dynamic behaviour of molecules and materials can be explored at the atomic scale, enabling the study of molecular interactions and complex physical and chemical processes. Central to the success of MD simulations is the availability of an energy function such as an empirical force field (FF) or more generally a potential energy surface (PES) to obtain the total energy of the system. In the case of FFs the function relies on empirically chosen mathematical functions and parameters, such as the popular CHARMM general force field (CGenFF) for drug-like molecules.^{4,5}

While traditional FFs have played a crucial role in advancing our understanding of molecular systems, they are not without limitations. One of the most notable challenges lies in

achieving a balance between accuracy and computational efficiency. This trade-off between accuracy and speed has been a persistent bottleneck in the field of atomistic simulations. Recent advances in machine learning (ML), particularly in the field of kernel-based and neural network (NN) methods, have revolutionised our ability to model molecular systems with unprecedented precision.⁶⁻⁸ Such machine learned PESs (ML-PESs) can be trained to reproduce the quality of the underlying quantum chemical reference data with remarkable accuracy. This also eliminates the need for extensive and time-consuming empirical parametrization.

Although ML-PESs reach extraordinary accuracies with respect to their *ab initio* reference, their computational cost still lies between *ab initio* techniques and traditional empirical FFs which compromises their applicability in long-time and large-scale MD simulations.^{6,9} Since the accurate computation of experimental observables - such as optical spectra, pair distribution functions, free energies, to name a few - requires sufficiently long and accurate MD simulations, even ML-based PESs eventually become impractical due to their slow evaluation speed. In addition, typical NN-based approaches suffer from poor extrapolation properties, in particular in regions not covered by training data. To address these issues the present work introduces small NN-based models for molecular PESs which speeds up training and in particular evaluation times by ~ 2 orders of magnitude for the systems considered. This constitutes a significant step forward in view of larger-scale, accurate, and resource-efficient MD simulations using ML-based energy functions.

To increase the computational efficiency in training and evaluating ML-PESs the present work proposes to combine reproducing kernel Hilbert space (RKHS) techniques with NN-based strategies which will be referred to as KerNN in the following. First, the approach is applied to H_2CO as a benchmark system. Next, KerNN is applied to two reactive systems including HeH_2^+ and the hydrogen oxalate anion (or deprotonated oxalic acid, $\text{HO}_2\text{CCO}_2^-$).

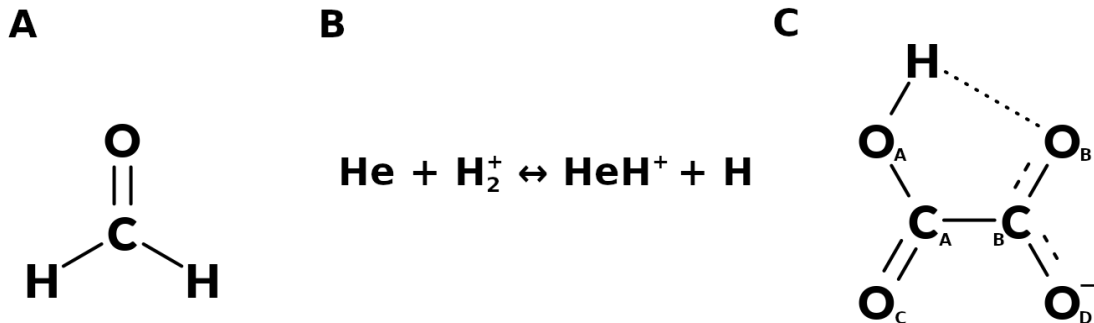


Figure 1: Schematic representation of A) formaldehyde, B) the two reaction channels of the HeH_2^+ system and C) hydrogen oxalate (or deprotonated oxalic acid) in its cyclic/hydrogen bonded form.

Schematics of the three molecular systems are given in Figure 1. Finally, the performance of KerNN in terms of accuracy, efficiency and robustness of the resulting simulations are presented and discussed in a broader context.

Results and Discussion

KerNN Architecture

KerNN is based on a small feed-forward NN with one input, two hidden and one output layer. The molecular descriptors are one-dimensional reciprocal power reproducing kernels, which effectively serve as a similarity measure between the interatomic distances of a reference and a query structure. Both, non-permutationally invariant (\mathcal{D}^{ns}) and permutationally invariant (\mathcal{D}^{s}) descriptors constructed from fundamental invariants¹⁰ are employed. The total potential energy of the system is KerNN’s output and forces are calculated via reverse mode automatic differentiation.¹¹ For spectroscopic applications, KerNN was adapted to predict dipole moments, too. Details are provided in the Methods section.

H₂CO

Training of KerNN for H₂CO was based on non-symmetrized \mathcal{D}^{ns} and symmetrized \mathcal{D}^{s} descriptors. Five independent repeats of training on different splits of the data and using four different data set sizes $N_{\text{Train}} = [400, 800, 1600, 3200]$ were carried out. The validation set invariably consisted of $N_{\text{Valid}} = 400$ structures while the hold-out test set contained the remaining $N_{\text{Test}} = N_{\text{Tot}} - (N_{\text{Train}} + N_{\text{Valid}})$ structures. Energy and force learning curves for KerNN^{ns} (NN employing the non-symmetrized descriptor \mathcal{D}^{ns} , given in Equation 10) and KerNN^s (NN employing the symmetrized descriptor \mathcal{D}^{s} , given in Equation 10) are shown in Figure 2.

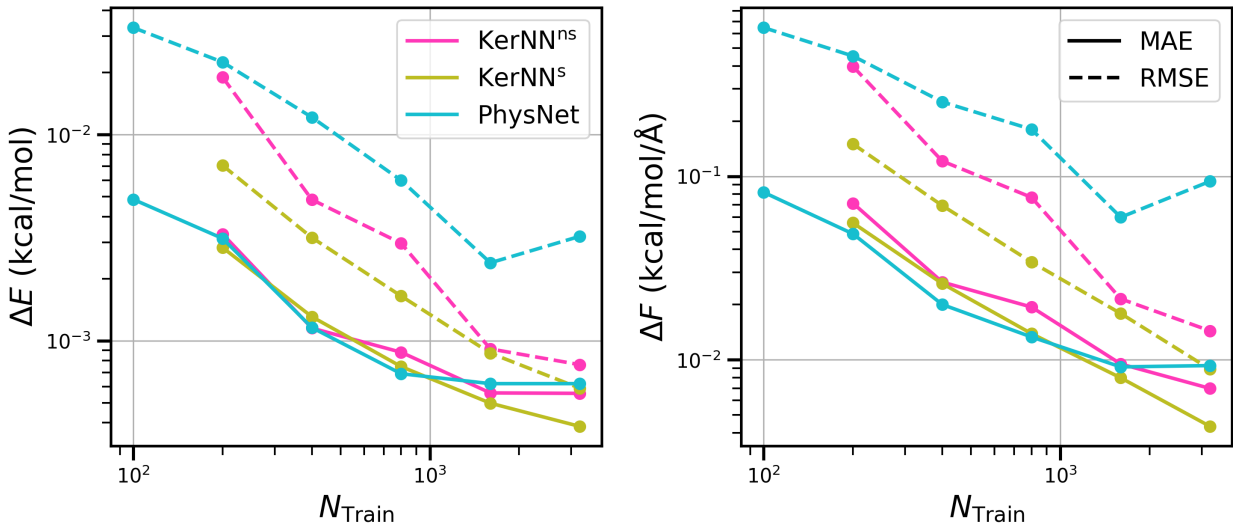


Figure 2: Energy and force learning curves for the different variants of the H₂CO PESs trained on CCSD(T)-F12B/aug-cc-pVTZ-F12 reference data. These are compared to PhysNet results taken from Reference 12. Solid and dashed lines represent MAEs and RMSEs, respectively. A total of five KerNN models were trained for each value of N_{Train} on different splits of the data and only the mean out-of-sample errors are shown. KerNN^{ns} and KerNN^s represent the NNs that use the non-symmetrized (\mathcal{D}^{ns}) and symmetrized (\mathcal{D}^{s}) descriptors, respectively. The flattening in energies for $N_{\text{Train}} \geq 1600$ is caused by the "error floor" noted in earlier work for the CCSD(T)-F12 forces.¹² Note that the different models can be more or less sensitive to such noise and therefore exhibit a flattening at higher/lower test set errors. The lowest test set MAEs reported in Reference,¹² for example, were $\text{MAE}(E) = 3\text{E-}4$ and $\text{MAE}(F)=1\text{E-}4$.

Learning curves quantify the rate at which ML models learn. It has been shown empirically¹³ that on average the test set errors must decay inversely with training set size N_{Train} according to a power law

$$\text{Error} \approx a/N_{\text{Train}}^b. \quad (1)$$

On a log-log plot, learning curves for ML models should therefore follow

$$\log(\text{Error}) \approx \log(a) - b \log(N_{\text{Train}}) \quad (2)$$

with an offset $\log(a)$ and a slope b .^{14,15} The learning curves in Figure 2 demonstrate that the logarithm of the error consistently decreases linearly for larger training set sizes for both, \mathcal{D}^{ns} and \mathcal{D}^{s} . This is particularly evident for the force learning curves. The quantity that was minimized during training was a mean squared error loss, in which the errors in the forces contributed ten times more ($\omega_F = 10$, see Table S1). Thus, the most meaningful comparison of the different models in Figure 2 is given by $\text{RMSE}(F)$ (right panel, dashed lines). Here, KerNN^s reaches the lowest out-of-sample errors throughout. Notably, the approach presented herein can also be compared to other state-of-the-art ML models in terms of out-of-sample errors on the same data set.¹² With $N_{\text{Train}} = 200$ the $\text{MAE}(F)$ ($\text{RMSE}(F)$) for the two KerNN variants are $7.1 \cdot 10^{-2}$, $5.5 \cdot 10^{-2}$ (0.40, 0.15) kcal/mol/Å, compared with $4.9 \cdot 10^{-2}$, $6.1 \cdot 10^{-2}$ and $5.1 \cdot 10^{-4}$ (0.45, 0.33 and $3.0 \cdot 10^{-3}$) kcal/mol/Å for PhysNet,¹⁶ RKHS+F¹⁷ and kernel ridge regression using the FCHL descriptor,¹⁸ respectively.

It is interesting to assess to what extent permutational invariance of the identical H-atoms impacts the predictions (E and \mathbf{F}) of KerNN^{ns} and KerNN^s. For KerNN^s the total energy is invariant upon exchange of the two H-atoms by construction, which is not guaranteed for KerNN^{ns} (or any other approach that is not permutationally invariant). However, for the optimized H₂CO configuration the energy of KerNN^{ns} remains unaltered upon H-exchange.

This is a consequence of the symmetry in the data and also because the small size of H₂CO helps to cover the relevant symmetry-related structures. A similar analysis can be carried out for forces by predicting them for a symmetric (C_{2v}) structure of H₂CO and comparing them to their *ab initio* counterparts. The analysis of the atomic MAE(\mathbf{F}), shown in Figure 3, illustrates that the atomic MAE(\mathbf{F}) are larger for the structure using KerNN^{ns}. Also, KerNN^{ns} fails to predict fully symmetric forces (with atomic MAE(\mathbf{F}) of 0.99 and 0.80 kcal/mol for the two H-atoms) whereas for KerNN^s the atomic MAE(\mathbf{F}) is identical on both H-atoms (0.39 kcal/mol).

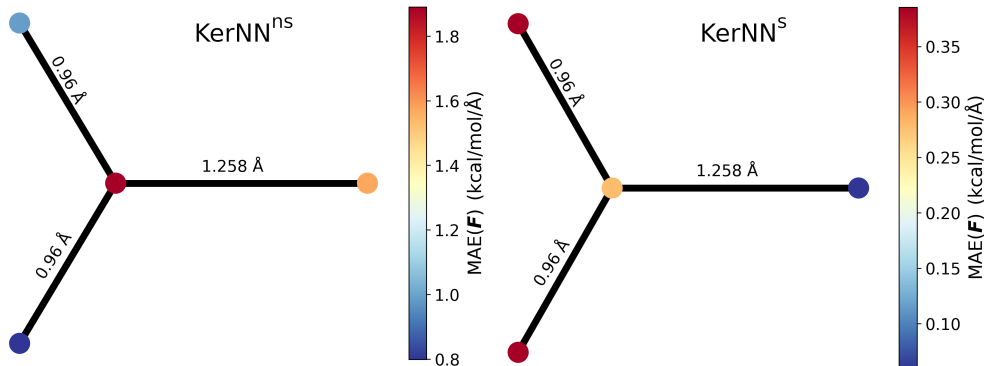


Figure 3: Atomic MAE(\mathbf{F}) (*i.e.* the mean absolute error between the reference and predicted forces for each of the atoms) for the symmetric structure with short H-C bonds shown. The corresponding (aggregated) MAE(\mathbf{F}) are 1.3/0.3 kcal/mol/Å. While KerNN^s predicts symmetrical errors, this is not so for KerNN^{ns}.

An additional test for the accuracy of the forces (or the curvature of the PES) around a stationary point are the harmonic frequencies. These are given in Table S3 and compared to their *ab initio* CCSD(T)-F12B reference and frequencies obtained from other ML approaches,¹² including PhysNet,¹⁶ RKHS+F¹⁷ and kernel ridge regression using the FCHL descriptor.¹⁸ KerNN^{ns} features excellent accuracy (MAE(ω)=0.2 cm⁻¹) and is competitive in comparison to both, KerNN^s and the more sophisticated (in terms of NN architecture, physically motivated terms such as electrostatics, number of parameters, descriptors that include distance and angular terms, *etc.*) ML approaches (MAE(ω)=0.1 cm⁻¹).

The previous evaluations focused on analyzing the models’ capability for interpolation, *i.e.*, how well they predict the properties of structures within (*e.g.*, energy- or interatomic distance-wise) their training data. A more challenging task, however, concerns the extrapolation capabilities of ML models. Reliable extrapolation is not at all guaranteed because such models are purely mathematical constructs without inherent physical meaning. Specifically for PESs to be used for dynamics simulations, poor extrapolation capabilities can lead to significant errors, potentially resulting in unphysical or incorrect behavior in areas of the energy landscape that are not covered by the training data. As was noted in References 19 and 20, low test set errors do not guarantee robust MD simulations. Hence, the extrapolation performance of both KerNN variants was considered, see Figure 4. The extrapolation dataset, shown in Figure 4A and available from previous work,¹² covers structures that were sampled at considerably higher temperatures (5000 K) than the training set (2000 K) and covers a much broader energy range (130 vs. 40 kcal/mol). Notably, KerNN^s extrapolates very accurately without any extreme outliers and has only small deviations at the highest energies. KerNN^{ns} closely follows the accuracy of KerNN^s with slightly larger deviations in the high energy range.

Meaningful extrapolation outside the range covered by the training/validation/test data is typically very challenging for ML models for both, NNs and kernel-based methods (depending on what descriptor is used). Both tend to behave unphysically and have increasingly large prediction errors in the extrapolation regime.⁶ An example is reported in Figure 4B which shows one-dimensional cuts through different PESs along a C-H bond of formaldehyde. The evaluation illustrates the robust extrapolation of both KerNN variants (magenta, olive) far beyond the training data whereas PhysNet (cyan) fails for bond lengths outside the training data set. As a comparison, two additional descriptors were employed for the same NN architecture as KerNN (non-symmetrized set of interatomic distances (r , gray-dashed) and non-symmetrized exponentials of the set of negative interatomic distances (e^{-r} , blue)).

It is conjectured that the long-range asymptotics of KerNN can be further adjusted and controlled by including targeted data from either *ab initio* calculations or experiments. This is valuable for situations in which electronic structure calculations fail to provide reliable reference data as can be the case for MRCI or CASPT2 calculations in the dissociation region.

To test this, the experimentally determined C-H dissociation energy (86.6 kcal/mol) was used to further constrain the long range part of the KerNN PES.²¹ Ten structures with a C-H distance of $\sim 10 \text{ \AA}$ were assigned with that energy and the model was transfer learned by fine-tuning the weights and biases of the KerNN^s PES. The energy of the empirical data points was set to $(-371 + 86.6 =) -284 \text{ kcal/mol}$ and is marked by a red line in Figure 4, to which the KerNN^s_{TL} is successfully corrected. It is noted that the *ab initio* reference data predicts a small barrier at $R_{\text{C-H}} \sim 3 \text{ \AA}$ and it is unclear if this a spurious barrier caused by using a single-reference method for a multi-reference problem. Such spurious barriers (or minima) can have detrimental effects on the dynamics of a molecular system.²² The reliable extrapolation capability of KerNN is likely a consequence of using kernels as descriptors since $k(r_i, r'_i)$ decays smoothly and monotonically towards zero for large r_i (see Figure S1). In other words, the guaranteed long-range decay of $k(r_i, r'_i)$ as a feature in the NN controls the global behaviour of the energetics and avoids arbitrary predictions outside the range covered by the training data. This is an essential advantage of KerNN over other NN-based and in part other kernel-based approaches.

Finally, KerNN can also be used to run finite-temperature MD simulations from which a multitude of experimental observables can be computed. Here, the infrared spectrum (IR) was determined which was also available from earlier studies of H₂CO using PhysNet¹² and from experiments.²³ For that reason, KerNN^{ns} was trained on energies, forces and dipole moments and its test set errors are given in Table S4. IR spectra were determined from the

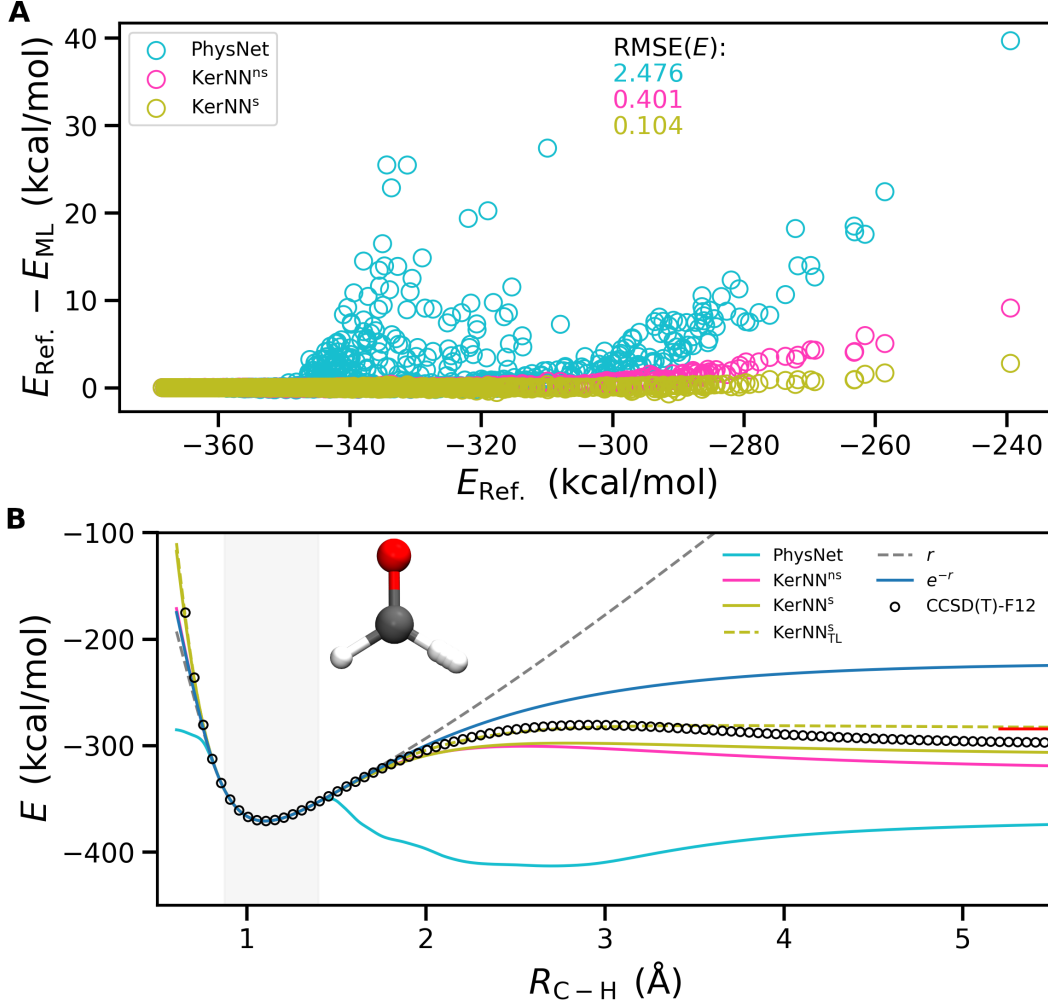


Figure 4: A: The extrapolation capabilities of the ML-PES are assessed on a data set containing 2500 structures, generated from normal mode sampling at a higher temperature (5000 K) than the training set (2000 K). The extrapolation data set was available from previous work.¹² While the training data covers an energy range of roughly 40 kcal/mol the extrapolation data set covers 130 kcal/mol. B: One-dimensional PES cut along the C-H bond length for different ML models (r and e^{-r} correspond to NNs with the same architecture as KerNN, but employing different descriptors, namely the interatomic distances r and e^{-r}). KerNN^s_{TL} corresponds to a model with asymptotic behaviour adjusted according to the experimentally determined dissociation energy. The training data range is shaded in gray.

Fourier transform of the dipole moment autocorrelation function²⁴ following

$$I(\omega)n(\omega) \propto Q(\omega) \cdot \text{Im} \int_0^\infty dt e^{i\omega t} \sum_{i=x,y,z} \langle \boldsymbol{\mu}_i(t) \cdot \boldsymbol{\mu}_i(0) \rangle. \quad (3)$$

The Fourier transform was multiplied by a quantum correction factor $Q(\omega) = \tanh(\beta\hbar\omega/2)$.²⁵ The dipole moment was that from the trained KerNN^{ns} model which incorporates effects due to atom-centered fluctuating charges. Unfortunately, learning the dipole moment by training on the extended loss function (7) is impossible for KerNN^s due to its permutational invariance (see Figure S2).

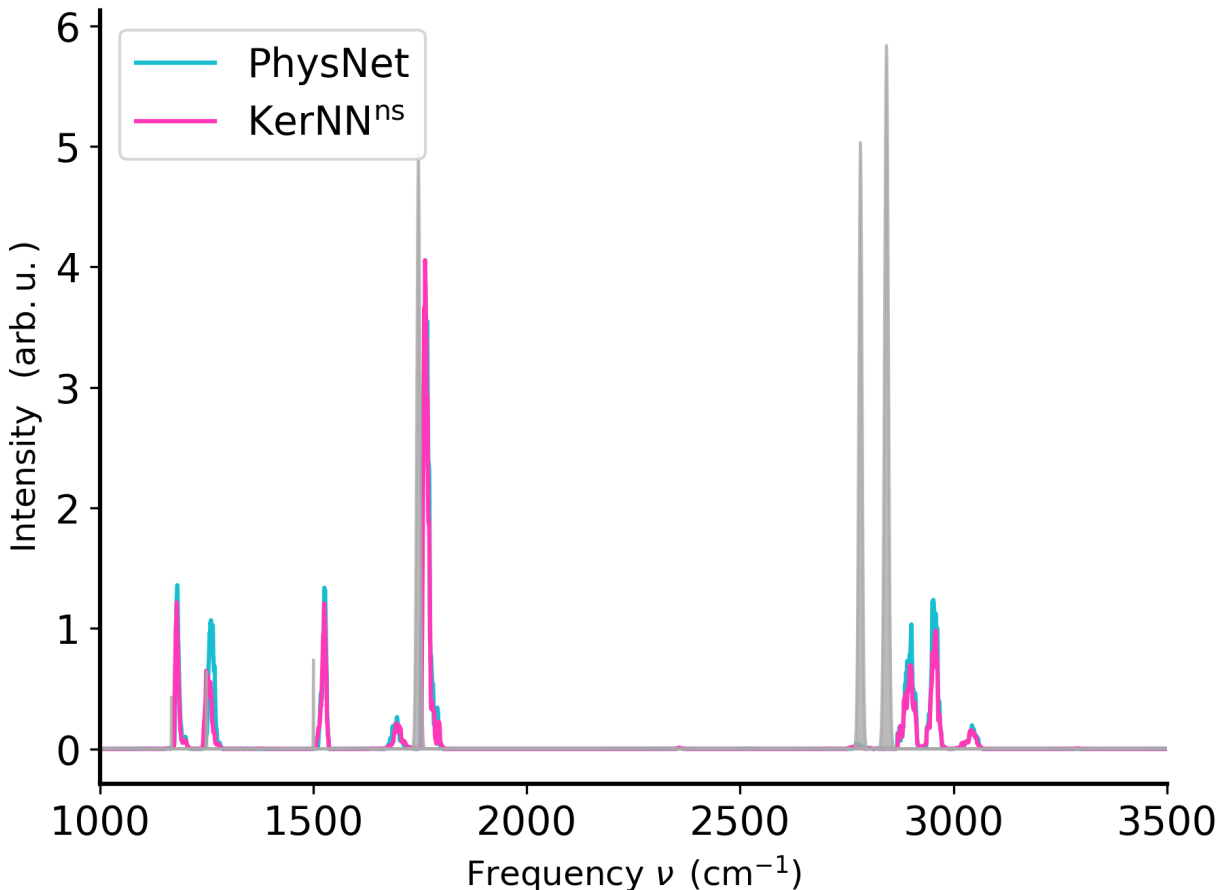


Figure 5: Infrared spectra derived from finite- T MD simulations of H_2CO . The experimental fundamentals²³ are the grey Gaussians. The computed spectra were averaged over 100 independent trajectories, each 200 ps in length, using $\Delta t = 0.2$ fs.

The MD simulations, carried out using the atomic simulation environment (ASE),²⁶ were each 200 ps in length, run with a time step of $\Delta t = 0.2$ fs to conserve total energy, starting from randomly initialized momenta drawn from a Maxwell-Boltzmann distribution at $T = 500$ K and using the optimized H_2CO structure as the initial configuration. Averaged

IR spectra determined from 100 independent simulations are shown in Figure 5. In terms of peak positions, the KerNN^{ns} and PhysNet spectra are indistinguishable, and only small differences in their intensities are found. In addition to the six fundamental bands, an overtone and a combination band are visible at ~ 2770 and 3040 cm^{-1} , respectively. Comparable to the computed IR spectrum, the experimental spectrum of pure formaldehyde ice²⁷ also shows a sideband on the red side of the 1725 cm^{-1} peak which, however, remained unassigned.

From a more technical perspective, the results so far are particularly remarkable and promising considering the small number of learnable parameters (1001 and 1021 for KerNN^{ns} and KerNN^s) the two KerNN approaches have. This compares with kernel-based methods that usually have one parameter per data point and NNs that can have millions of parameters. The compact form and resulting inference speed of KerNN is the advantage of such approaches and their computational cost for energy and force evaluations is given in Table S5. KerNN in its Python implementation is roughly 15 (50) times faster than PhysNet (kernel ridge regression with FCHL), and only slightly slower than RKHS+F, which is written in FORTRAN.^{17,28} If KerNN’s FORTRAN implementation is used (*e.g.*, from within CHARMM), this yields a 100-fold speedup over its Python implementation and, therefore, outperforms PhysNet by orders of magnitude. Compared with RKHS+F, the compact NNs are 20 to 30 times faster allowing considerably longer simulation times at comparable accuracy. Notably, if the training set size is increased (as would likely be necessary for larger molecules), the computational cost of an E and \mathbf{F} evaluation remains the same for KerNN, whereas it scales quadratically with the training/reference data for RKHS+F and the matrix inversion for obtaining the linear coefficients scales cubically which becomes prohibitive for reference data larger than $\sim 10^4$.

HeH₂⁺

Next, KerNN was applied to a reactive system: $\text{He} - \text{H}_2^+ \rightarrow \text{HeH}^+ + \text{H}$. Breaking and forming chemical bonds requires a *globally valid* PES, as opposed to a local PES as was the case for H₂CO, which is generally more challenging. Again, two descriptors, \mathcal{D}^{ns} and \mathcal{D}^{s} were used and one model was trained for each of them. Because only numerical gradients were available at the UCCSD(T) level of theory, weighting force contributions in the loss was reduced to $\omega_F = 1$. Hence, the focus was put more on validations of energetics and observables that can be derived from them. Nevertheless, test set errors on forces and harmonic frequencies (see Table S6) were still determined.

Following the standard practice for assessing the performance of ML-based PESs, the test set errors were evaluated. From the full reference data set, 4709 random structures were excluded from the training. The energy and force prediction errors together with their averages on the test set for KerNN^{ns} and KerNN^s are shown in Figures 6A and B. The energies are predicted with high fidelity ($\text{MAE}(E) < 0.01$ kcal/mol for both KerNN variants). KerNN^s has slightly larger averaged errors than KerNN^{ns}, which is likely due to the variability in the training process. While most predictions were within 0.1 kcal/mol of their *ab initio* reference values, single outliers with $0.5 < \Delta E < 2.0$ kcal/mol exist. The three structures with the largest errors are shown in Figure S3. Two out of three outliers are the same in KerNN^{ns} and KerNN^s and both structures feature large interatomic distances ($r(\text{He} - \text{H}) \geq 2.3$ Å) with comparable H-He-H angle. Structures close to full dissociation are likely to pose a challenge for single reference methods such as UCCSD(T). This can be verified by comparing energies from UCCSD(T) and FCI calculations for selected structures. It is noted that for a three-electron system CCSDT and FCI are equivalent which implies that UCCSD(T) is close but not identical to these highest-accuracy methods. The two structures considered were the equilibrium configuration determined on KerNN^{ns} (linear [He-H-H]⁺) and the structure with the largest ΔE between reference calculations and KerNN^{ns} which is partially dissoci-

ated. At the minimum the energy difference $\Delta_{\text{UCCSD(T)/FCI}} = 0.02$ kcal/mol compares with $\Delta_{\text{UCCSD(T)/FCI}} = 1.40$ kcal/mol for the outlier structure. This is a clear indication for the difficulty of UCCSD(T) to describe geometries close to dissociation correctly. It is interesting to note that the prediction error of KerNN is ~ 1.5 kcal/mol (see Figure 6A and B), which is comparable to $\Delta_{\text{UCCSD(T)/FCI}}$. This also implies that KerNN can identify irregularities in the data set.

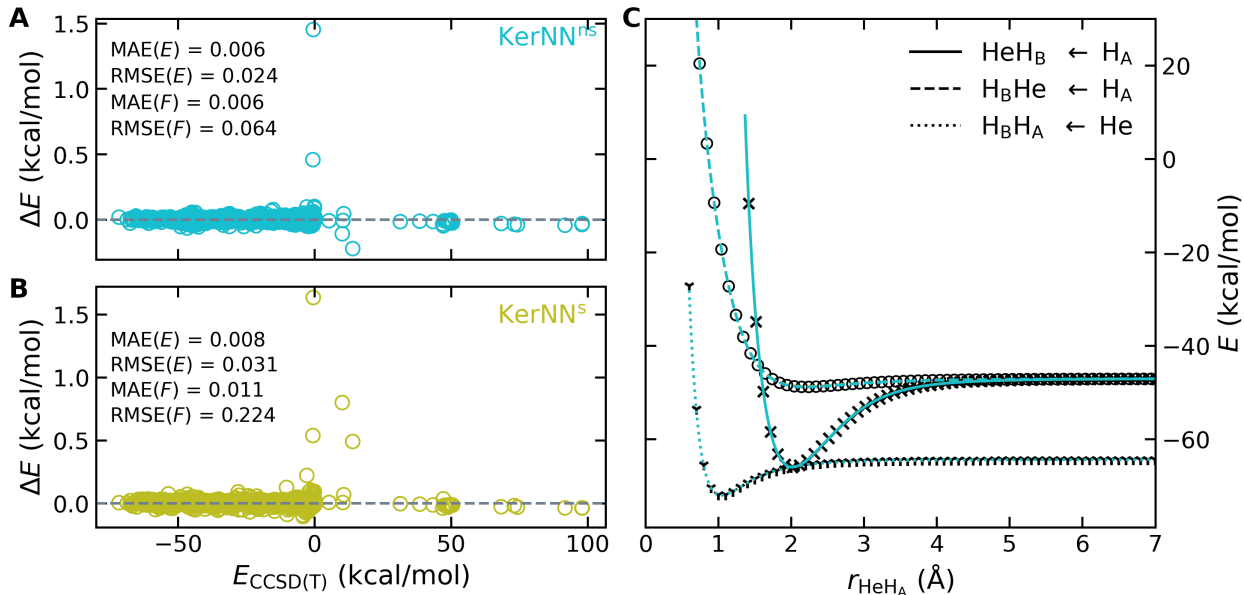


Figure 6: Out-of-sample errors for the HeH_2^+ KerNN^{ns} (A, cyan) and KerNN^s (B, olive) PESs (with \mathcal{D}^{ns} and \mathcal{D}^{s} as descriptors, respectively) trained on UCCSD(T)/aug-cc-pV5Z level reference data. The test set contains 4709 randomly chosen structures. Most energies are predicted with errors well below 0.1 kcal/mol, while single outliers exist (see text). C: One-dimensional potential energy scan along r_{HeH_A} for a collinear approach of the reactants as determined on KerNN^{ns} (cyan). $\text{HeH}_B \leftarrow \text{H}_A$ refers to diatomic HeH_B at its optimized bond length with H_A approaching atom H_B . The scans for KerNN^s are shown, too, but are overlapped by the KerNN^{ns} results. Three different atomic arrangements are shown and *ab initio* energies determined at the UCCSD(T)/aug-cc-pV5Z are illustrated as black symbols. The zero of energy was taken with respect to the free atoms.

Figure 6 (C) shows one-dimensional potential energy scans along r_{HeH_A} as determined on the KerNN PESs for three different collinear approaches. The one-dimensional potential energy scans are shown for the KerNN PESs using \mathcal{D}^{ns} and \mathcal{D}^{s} . The results (cyan and olive lines) are

so close that they overlap on the scale of the plot. Black symbols represent explicit *ab initio* UCCSD(T) energies using the same grid as for scanning the KerNN PESs. The exceptional quality of the KerNN PESs is apparent both, for the short and the long-range part of the PES. The maximum differences between the PESs and the *ab initio* reference energies for all scans are < 0.1 kcal/mol and emphasize the accuracy of the PESs. In addition to probing the bond formation process in one dimension in Figure 6, the accuracy of the reactive KerNN^{ns} PES, in particular for the He + H₂⁺ and HeH⁺ + H channels, is shown in Figures S4 and S5. The comparison to direct UCCSD(T) calculations yield MAE(E) of 0.05 and 0.70 kcal/mol for the He + H₂⁺ and HeH⁺ + H channels, respectively. Excluding the ten predictions with the largest error for the latter (located exclusively in the repulsive region) yields a MAE(E) of 0.06 kcal/mol. KerNN is also suitable to investigate chemical reactions, see Figure S6. Here two exemplary trajectories, one non-reactive (A) and the other one reactive (B) using KerNN^{ns} are shown.

As an application of the KerNN PESs the ro-vibrational energies for the He–H₂⁺ ionic complex were determined for the KerNN^{ns} PES using the DVR3D suite of programs²⁹ which solves the three-dimensional Schrödinger equation in a discrete variable representation (DVR) for a given PES. Due to the considerable stabilization of the He–H₂⁺ ionic complex it is well approximated as a semi-rigid system with vibrational modes ($\nu_1, \nu_2, \nu_3 \equiv \nu_r, \nu_b, \nu_s$). In a local mode picture, these are the H–H⁺ stretch, He–H–H⁺ bend and the He–H₂⁺ stretch modes, respectively.

Ro-vibrational bound states were determined for *ortho-/para*-HeH₂⁺ for total angular momentum $J = 0, 1$ in *e/f* parity for the complex. Because *o-/p*-H₂⁺ only populates odd/even j -states, the dissociation limits for the two species differ by $2B = 59.9$ cm⁻¹ at the UCCSD(T) level of theory, where B is the rotational constant of H₂⁺. A comprehensive list of all calculated states considered is given in Table S7, which compares results from

using the KerNN^{ns} PES with earlier calculations performed on a FCI/aug-cc-pV5Z RKHS PES.³⁰ The difference between the earlier and the present predictions of the bound state energies are given in Figure S7. The ground state energies of *o*- and *p*-H₂⁺ ($\nu = 0, j = 0$)-He determined on the KerNN^{ns} PES are -1793.3578 and -1793.3585 cm⁻¹, which are within less than 0.5 cm⁻¹ from the energies determined on the FCI PES which are -1793.7632 and -1793.7639 cm⁻¹. Comparing all 64 states from the KerNN^{ns} and the RKHS PES it is evident that KerNN^{ns} typically underestimates the bound state energy in comparison to the FCI PES (*i.e.*, predicts it at lower wavenumber). While this is not the case for the states with the lowest n it is invariably the case for states with $n > 4$. Notably, the underestimation increases for near-dissociative bound states (for increasing n). Among all states, the maximum deviation between KerNN^{ns} and RKHS is ~ 6 cm⁻¹ with a MAE of 2.5 cm⁻¹.

Several transition frequencies were recently characterized experimentally for the first time from low-resolution spectra in an ion trap at 4 K using a free electron laser, see Table 1.³¹ With the help of ro-vibrational calculations on the FCI-RKHS PES³⁰ the experimentally detected peak at 1840 cm⁻¹ was assigned to the H₂⁺ stretch whereas the peaks at 695 and 840 cm⁻¹ correspond to the He-H₂⁺ bend and van der Waals stretch modes. These compare with computed transition frequencies of 1809/1829, 641, and 729 cm⁻¹ from DVR3D calculations using the KerNN^{ns} PES which differ by only a few cm⁻¹ from the bound state calculations using the RKHS-FCI PES. For the former transition frequency (1809/1829), there are two states because they couple with the bend and stretch modes of the complex. When comparing computed and experimentally reported transition frequencies one must note that the widths of the measured spectra can be considerable, e.g. ~ 100 cm⁻¹ for the H₂⁺ stretch fundamental, with appreciable uncertainty of ~ 10 cm⁻¹ in the position of the maximum. Also, there is a shoulder ~ 20 cm⁻¹ to the red of the measured fundamental transition at 1840 cm⁻¹, which is nicely captured by the calculations (*i.e.*, 1829 and 1809). Furthermore, two low-intensity peaks at 1159 and 1234 cm⁻¹ can be identified as the (0200) and (0020)

overtones using the calculations, which are within 30 and 20 cm^{-1} of the computations, respectively.

Table 1: Measured³¹ and calculated³¹ vibrational transition frequencies for HeH_2^+ . The fundamentals are (010), (001), and (100) for the bend, van der Waals stretch, and H_2^+ stretch modes. The CCVM calculations³¹ were carried out on the RKHS representation of the FCI energies³⁰ and the DVR3D calculations used the KerNN^{ns} representation of the UCCSD(T) data. Transition frequencies are given for ortho-[para-] H_2^+ separately. It is demonstrated that the differences between ortho- and para-energies for the two calculations are identical throughout.

ν_1	ν_2	ν_3	k'	Exp. ³¹	CCVM/RKHS(FCI) ³¹	DVR3D/KerNN ^{ns} (UCCSD(T))
0	1	0	1	695	640 [640]	640.7 [640.7]
0	0	1	0	840	731.6 [731.6]	729.1 [729.1]
0	2	0	0	1159	1136.1 [1134.1]	1134.8 [1132.8]
0	0	2	0	1234	1256.4 [1255.6]	1252.1 [1251.3]
1	0	0	0	1840	1812/1833	1808.6/1829.3

Comparing the theoretical predictions carried out on two different PESs based on different levels of theory (FCI vs. UCCSD(T)), two different representations (RKHS and KerNN), and using two different methods for computing bound states (CCVM and DVR3D) shows excellent agreement. This indicates that both calculations are consistent and precise. This is very encouraging and lends considerable credibility to a computational approach for predicting spectroscopic properties of experimentally challenging systems. The RKHS-FCI PES has also been successfully used together with wavepacket simulations to characterize Feshbach resonances in He-H_2^+ .³²⁻³⁴ While the experiment and the theoretical calculations are in reasonable agreement, this calls for additional high-resolution experiments, for which the theoretical predictions can serve as valuable benchmark.

Hydrogen Oxalate

As a final application of KerNN the spectroscopy and reaction dynamics of hydrogen oxalate are followed. The infrared spectroscopy of hydrogen oxalate has been characterized from both, experiments and computations.^{35,36} The system is highly symmetric, has a strong intramolecular hydrogen bond and features a corresponding hydrogen transfer. The system serves as a test case to assess the feasibility for larger, reactive systems. Therefore, only a KerNN^{ns} was trained and a corresponding PhysNet model was generated based on the same training data. The quality of the two PESs on the corresponding test sets is reported in Figure 7 and MAE and RMSE are summarized in Table S8. It is found that across the full range of energies covered the KerNN^{ns} PES is competitive with PhysNet despite the fact that the number of free parameters for PhysNet is larger by more than two orders of magnitude. In fact, for certain properties (RMSE(E), RMSE(F), MAE(μ), and RMSE(μ)) KerNN^{ns} performs better than PhysNet.

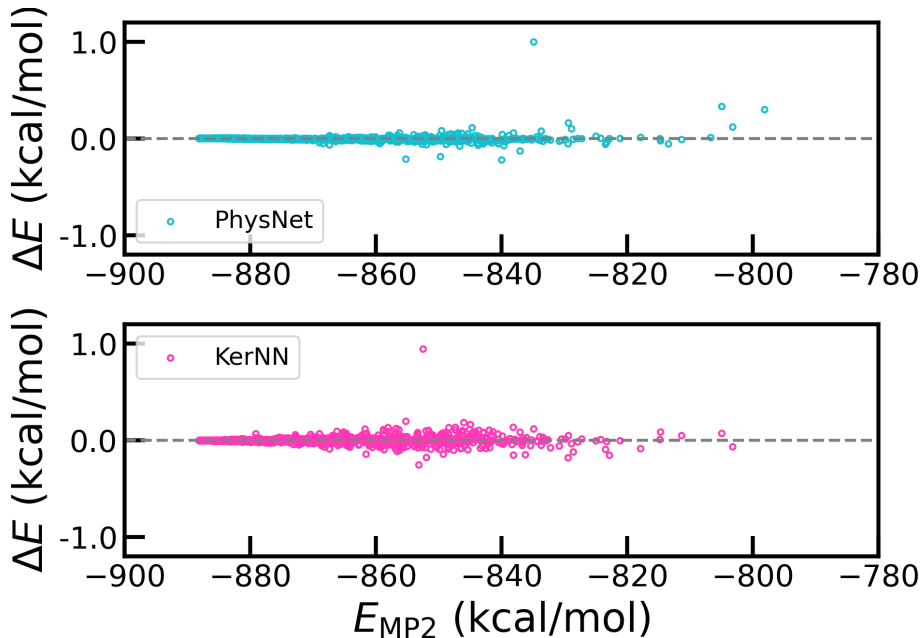


Figure 7: Out of sample errors on a test set containing 2000 hydrogen oxalate structures for the KerNN^{ns} and PhysNet PESs.

To study the spectroscopy and dynamics of hydrogen oxalate, MD simulations were carried out using ASE²⁶ for both KerNN^{ns} and PhysNet. A total of 100 simulations were started from the same initial conditions for each of the energy functions. Initially, the molecule was optimized and random momenta were drawn from a Maxwell-Boltzmann distribution corresponding to 300 K and assigned to each of the atoms. The MD simulations were propagated in the *NVE* ensemble using the velocity Verlet algorithm with a time step of 0.2 fs for 10⁶ steps. This aggregates to a total of 20 ns simulation time for each of the PESs.

The infrared spectra determined from the MD simulations described above are reported in Figure 8. The framework modes below 2000 cm⁻¹ were all captured rather accurately compared with experiment. It should be noted that the PESs are based on the MP2 level of theory and that the experiments were carried out using the H₂-messenger technique which, strictly speaking, is not a gas phase spectrum. Nevertheless, the interaction between the H₂-messenger and hydrogen oxalate is still weak so that only small perturbations are expected. A notable feature is that the two computed spectra from using PhysNet and KerNN (cyan and magenta traces, respectively) are rather close to one another, except for a peak at 1380 cm⁻¹ which appears only for KerNN^{ns} but is consistent with experiments (olive trace). In other words, the KerNN^{ns} PES is demonstrably of the same quality as the PhysNet model - if not even superior. The relative intensities between experiment and simulations are probably influenced by the fact that experimentally, a H₂ tagging technique was employed whereas the simulations are in the gas phase. For the most interesting spectral feature below 3000 cm⁻¹ the two simulations agree as well and allow to assign the measured/calculated pronounced maximum around 2930/3050 cm⁻¹ to the O-H stretch or proton transfer mode. In the experiment, a characteristic plateau with signals between 2600 and 2900 cm⁻¹ was detected. This signal range is also detected in the simulations, albeit with a different intensity pattern. This is in contrast to earlier work on the vibrational spectroscopy and dynamics of hydrogen oxalate, which was based on a force field and was unable to reveal the width of the

plateau.³⁶ This is an advantage of ML-based PESs over traditional force fields as the former include all inter-mode couplings by learning them directly from *ab initio* reference data.

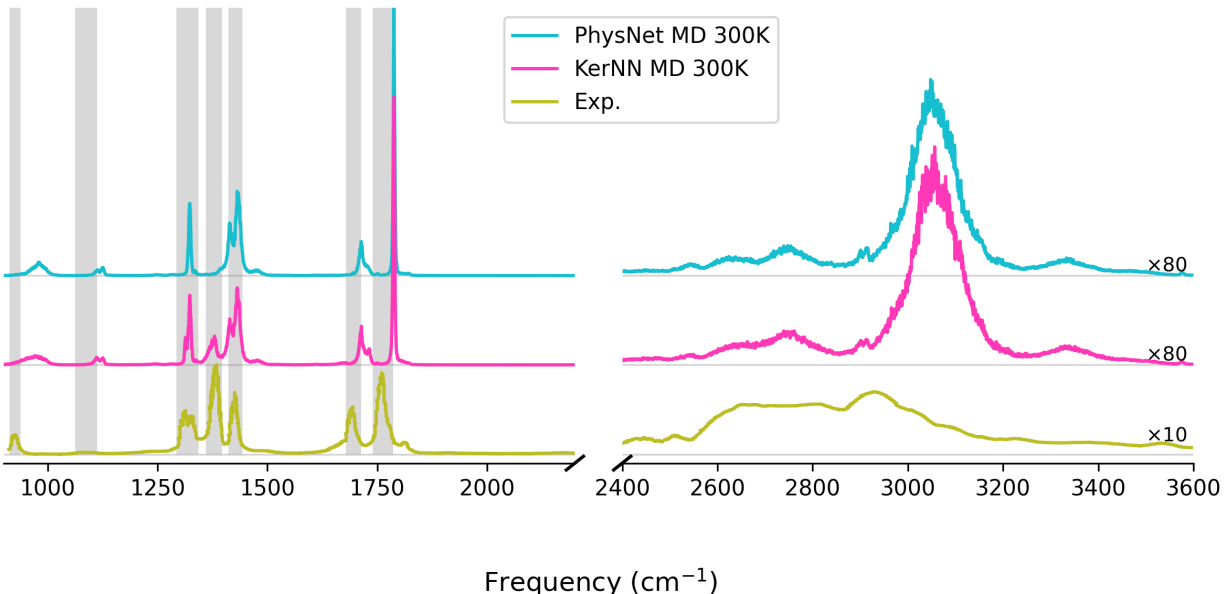


Figure 8: Infrared spectra of hydrogen oxalate. The computed spectra (top two traces) are obtained from the Fourier transform of the dipole-dipole autocorrelation function for MD simulations run with KerNN^{ns} and PhysNet. The bottom trace corresponds to an experimentally determined (H_2 -tagged) gas phase spectrum.³⁵ The grey-shaded areas correspond to the experimentally determined peak positions.

Finally, the same MD simulations that were employed to determine the IR spectra were used to calculate the hydrogen transfer rates. The barrier height for hydrogen transfer from reference MP2/aug-cc-pVTZ calculations is 2.355 kcal/mol which is closely reproduced by KerNN^{ns} (2.360 kcal/mol) and PhysNet (2.355 kcal/mol), respectively. From an aggregate of 20 ns MD simulation (100 independent simulations each 200 ps in length), 427 and 524 hydrogen transfers were observed from simulations using the KerNN^{ns} and PhysNet PESs. This corresponds to transfer rates of 21/ns and 26/ns. Malonaldehyde, which also features intramolecular hydrogen transfer between two adjacent O-atoms and is very similar to hydrogen oxalate, features a H-transfer barrier of 2.79 kcal/mol at the MP2/aug-cc-pVTZ level. The proton transfer dynamics of malonaldehyde has been studied in Reference 37,

which suggested that an O-O motion is gating the H-transfer. At 300 K, a transfer rate of 7.6/ns was reported. Acetoacetaldehyde/acetylacetone (both being methyl-substituted variants of malonaldehyde) which was also studied in earlier work has a H-transfer barrier of 2.59/2.17 kcal/mol at the MP2/aug-cc-pVTZ level, for which a transfer rate of 15/36 per ns was found and is consistent with the present findings.

As long as the hydrogen oxalate remains in its hydrogen-bonded form and the hydrogen atom transfers between the two oxygen atoms O_A and O_B (see Figure 1) for which training data is available the simulations are robust and meaningful. However, since the hydrogen-bond can break at elevated temperatures and a rotation about the C_A-C_B bond is possible, exchange of the hydrogen atom to O_C or O_D also becomes possible. Since the features are not symmetrized, the trajectory breaks down in such situations. This was not the case for MD simulations at 300 K. One remedy would be to cover the relevant symmetries with additional data ("data augmentation") or by including full or approximate permutational invariance into the model.

Conclusion and Outlook

The present work introduces KerNN to represent reactive and non-reactive potential energy surfaces. KerNN capitalizes on the idea that one-dimensional reproducing kernels provide accurate and asymptotically meaningful representations suitable for featurization of a (small) neural network. The main reason to explore such a combination was the realization that typical present-day NN-based PESs are over-parametrized by several orders of magnitude. It was shown in the present case that a KerNN with $\sim 10^3$ performs on par with a PhysNet model with $\sim 10^6$ parameters trained on the same reference data set. Occam's razor and the principle of parsimony state that among competing explanations the simplest explana-

tion with the fewest variables should be favoured.^{38,39} Such considerations also lead other fields, e.g. natural language processing⁴⁰ or computer vision,⁴¹ to consider the performance of smaller NN-architectures as has been done for KerNN in the present work. Apart from being resource-efficient in terms of training times, evaluation times, memory requirements and reduced concomitant energy consumption, small NN-based models may also offer advantages when moving towards explainable and interpretable models (XAI).

Using symmetrized and unsymmetrized descriptors, \mathcal{D}^s and \mathcal{D}^{ns} , offers advantages and disadvantages. For example, for symmetric structures of a symmetric molecule (H_2CO) forces on symmetry-equivalent atoms are exactly the same if the descriptor is symmetric. On the other hand the training and inference of KerNN^s is computationally more demanding than for KerNN^{ns} and the differences will be more pronounced in larger systems. This and the (almost) identical performance of the two models for H_2CO raises the question if a rigorous inclusion of physical constraints (such as the exact permutational invariance of like atoms) is mandatory. Recent work on the effect on broken symmetries, in particular for rotations, in ML come to similar conclusions and find that “[..]Despite the unquestionable appeal of incorporating fundamental physical concepts in the architecture of machine-learning models, it might be beneficial – and it certainly is not as detrimental one would expect – to just let models learn[.]”⁴² For KerNN applied to larger molecules, it will therefore be interesting to assess whether approximate permutational invariance, *e.g.* by data augmentation or by including permutational invariance only for “physically accessible” permutations, offers advantages over a more rigorous inclusion of permutational invariance. In addition, it may be possible to use kernels for describing the atomic environment to further generalize KerNN.

The extrapolation capabilities of KerNN were demonstrably excellent. This is a particular advantage for investigating bond-breaking and bond-formation. This property is also very advantageous for reference data from methods that are known to feature unpredictable con-

vergence, in particular in the asymptotic regions of the PES, such as multi-reference CI^{30,43,44} or if experimental data is available.

A particular advantage over Python-based methods is the fact that KerNN can be implemented in Fortran which (usually) is computationally more efficient. This is particularly relevant for long-time simulations of large systems, which require a large number of sequential force predictions. As all other NN-based methods, no explicit analytical form of the underlying model is assumed and coupling between internal degrees of freedom are explicitly incorporated into the model. This is of particular interest when energy transfer phenomena are studied. Future extensions of KerNN include the combination with accurate electrostatic models such as MDCM, fMDCM or kMDCM or multipolar electrostatics for modeling condensed phase systems.

In summary, the present work introduces an efficient and accurate approach to represent reactive and non-reactive molecular PESs. KerNN was applied to infrared spectroscopy and H-transfer reactions for systems with up to 6 heavy atoms. Extensions to larger molecules are possible but may require modifications in the kernels used. The most important insight of the present work is that considerably smaller and simpler ML-based models can be conceived without compromising their accuracy.

Methods

This section describes the reference data generation, followed by the NN architecture and the descriptors used.

***Ab initio* Data**

H₂CO: The *ab initio* reference data for H₂CO was available from previous work.¹² The data set contains a total of 4001 configurations generated using normal mode sampling⁴⁵ including the optimized H₂CO structure. *Ab initio* energies, forces and dipole moments were obtained for all structures at the CCSD(T)-F12B/aug-cc-pVTZ-F12 level of theory using MOLPRO.⁴⁶ To capture the equilibrium, room temperature, and higher energy regions of the PES, the normal mode sampling was carried out at eight different temperatures (10, 50, 100, 300, 500, 1000, 1500, and 2000 K). For each temperature, 500 structures were generated. For training, the energy is taken with respect to free atoms.

HeH₂⁺: The reference structures for the HeH₂⁺ system were generated on a grid using Jacobi coordinates (r, R, θ) where r is the bond length between diatomic species (either H₂⁺ or HeH⁺), R is the distance between the center of mass of the diatom and the third atom (either He or H) and θ is the angle between \vec{r} and \vec{R} . The details for the radial and angular grids for the reference structure generation are given in Table S2. Structures with any interatomic distance smaller than 0.6 Å were discarded. These are complemented with 500 structures obtained from running *NVT* MD simulations at 1500 K using the semiempirical GFN2-xTB method⁴⁷ for each of the diatomic species (the third atom was placed sufficiently far away). *Ab initio* energies and forces were determined at the UCCSD(T)/aug-cc-pV5Z level of theory for all structures. Since only numerical gradients were available for the UCCSD(T) method in MOLPRO, less relative weight is given to the forces during training (see Table S1). Structures with energies 100 kcal/mol or higher than the complete dissociation (*i.e.*, [He + H + H]⁺) were excluded, yielding a total of 62834 structures. The zero of energy was taken with respect to the free atoms (*i.e.*, [He + H + H]⁺ is at 0 kcal/mol).

Hydrogen oxalate: Structures for hydrogen oxalate were sampled by running *NVT* MD simulations at multiple temperatures (100, 300, 500, 1000 and 1500 K) using the semiem-

pirical GFN2-xTB method⁴⁷ (2500 structures each except for 1500 K for which only 1000 geometries were generated) as implemented in ASE.²⁶ The region around the proton transfer transition state was sampled with an artificial harmonic potential (1500 structures) and at $T = 500$ K. Additionally, normal mode sampling⁴⁵ at increasing temperatures (100, 300, 500, 100, 1500, 2000 K) was carried out for both the optimized and transition state structure of hydrogen oxalate (800 per T). The data set was augmented based on adaptive sampling and diffusion Monte Carlo simulations^{48,49} using PhysNet¹⁶ to ensure robustness of the PES. The final data set contained a total of 22110 structures, for which energies, forces and dipole moments were determined at the MP2/aug-cc-pVTZ level of theory using MOLPRO.⁴⁶ Again, the energy was taken with respect to free atoms.

Neural Network

The PESs for the three molecular systems were represented by a small and fully connected feed-forward NN. The fundamental building blocks of NNs are dense layers of the form

$$\mathbf{y} = \sigma(\mathbf{W}\mathbf{x} + \mathbf{b}), \tag{4}$$

which need to be stacked and combined with a non-linear activation function σ to model non-linear relationships within the data. Here, $\mathbf{x} \in \mathbb{R}^{n_{\text{in}}}$ ($\mathbf{y} \in \mathbb{R}^{n_{\text{out}}}$) corresponds to the input (output) vector with a dimensionality of n_{in} (n_{out}) and the activation is applied entry-wise. $\mathbf{W} \in \mathbb{R}^{n_{\text{out}} \times n_{\text{in}}}$ and $\mathbf{b} \in \mathbb{R}^{n_{\text{out}}}$ are the weights and biases that are learnable parameters. The NN architecture used throughout this work was

$$V = \mathbf{W}_3\sigma(\mathbf{W}_2\sigma(\mathbf{W}_1\sigma(\mathbf{W}_0\mathbf{k}(\mathbf{r}) + \mathbf{b}_0) + \mathbf{b}_1) + \mathbf{b}_2) + b_3, \tag{5}$$

and consists of an input (0), two hidden (1 and 2), and an output (3) layer. The activation function σ was a soft plus function, and the last layer was a linear transformation. The

input to the NN are functions of the interatomic distances $\mathbf{k}(\mathbf{r})$ (*vide infra*) and the output is the potential energy E of the molecule. The forces acting on the atoms were obtained from reverse mode automatic differentiation.¹¹

The learnable parameters of the NN were optimized by minimizing an appropriate loss function \mathcal{L} using AMSGRAD.⁵⁰ Here, a mean squared error loss was used and the loss function was

$$\mathcal{L} = |E - E^{\text{ref}}| + \omega_F \sum_{i=1}^N \sum_{\alpha=1}^3 \left| -\frac{\partial E}{\partial x_{i,\alpha}} - F_{i,\alpha}^{\text{ref}} \right|. \quad (6)$$

E and E^{ref} correspond to the model and reference energies, $F_{i,\alpha}^{\text{ref}}$ are the Cartesian components of the reference forces on atom i , and $x_{i,\alpha}$ is the α th Cartesian coordinate of atom i . ω_F is a hyperparameter to weigh the contribution of the forces to the total loss function. During training, an exponential moving average of all learnable parameters was tracked using a decay rate of 0.999. Overfitting was prevented using early stopping: After every epoch, the loss function was evaluated on a validation set of reference structures using the parameters obtained from the exponential moving average.⁵¹ After training, the model that performed best on the total validation loss (Equation 6 or 7 depending on whether dipole moments are required) was selected.

If a dipole moment surface was desired, *e.g.*, for spectroscopic studies, the same NN can be used with only little adaptation. First, the number of output nodes needs to be changed to $N_{\text{atoms}} + 1$ (one for the energy and one each for atomic partial charges q_i). Inspired by PhysNet¹⁶ (and similar NNs) and given that the dipole moment is $\boldsymbol{\mu} = \sum_{i=1}^{N_{\text{atoms}}} q_i \mathbf{x}_i$, the

loss function is changed to

$$\mathcal{L} = |E - E^{\text{ref}}| + \omega_F \sum_{i=1}^N \sum_{\alpha=1}^3 \left| -\frac{\partial E}{\partial x_{i,\alpha}} - F_{i,\alpha}^{\text{ref}} \right| + \omega_\mu \left| \sum_{\alpha=1}^3 \sum_{i=1}^N q_i x_{i,\alpha} - \mu_\alpha^{\text{ref}} \right| + \omega_Q \left| \sum_{i=1}^N q_i - Q^{\text{ref}} \right| \quad (7)$$

where q_i is the partial atomic charge of atom i , Q^{ref} is the total charge of the system and ω_μ and ω_Q are the corresponding hyperparameters.

Descriptors

The design of molecular descriptors (*i.e.*, encoding a molecular configuration in a machine-readable format) is a pertinent problem in quantum ML and an active area of research.⁵² Such descriptors ideally satisfy several key criteria including (i) invariance under transformations such as translation, rotation, and permutation of identical elements, (ii) uniqueness, exhibiting changes when transformations that alter the predicted properties are applied, and (iii) continuity and differentiability with respect to atomic coordinates to enable the calculation of forces in molecular simulations.⁷ Descriptors can typically be categorized into two groups: fixed or learnable descriptors.⁵³

While translational and rotational invariance are straightforward to satisfy by resorting to internal coordinates, permutational invariance is more challenging to achieve. Many high-dimensional NNs obtain atomic contributions to a total energy, which satisfies the permutational invariance by construction.^{16,54} Alternative routes to permutationally invariant PESs include data augmentation,⁵⁵ symmetrization of NNs,^{56,57} or input symmetrization.^{58,59} The latter is frequently achieved by using a permutation invariant basis to generate permutationally invariant polynomials, which were applied successfully to numerous systems.^{60–62} However, including the permutational invariance into a PES usually requires a large func-

tion space for fitting and the transformed, symmetrized basis will be larger than (or equal to) the original vector space.

The descriptors used here are based on concepts rooted in the theory of reproducing kernels^{17,28,63,64} which have also been successfully employed for representing reactive PESs for small molecules.^{30,44,65,66} One-dimensional reciprocal power reproducing kernels

$$k^{[n,m]}(x, x') = n^2 x_{>}^{-(m+1)} B(m+1, n) {}_2F_1\left(-n+1, m+1; n+m+1; \frac{x_{<}}{x_{>}}\right) \quad (8)$$

were shown to represent diatomic potentials faithfully.^{64,67} In Eq. 8 $x_{<}$ and $x_{>}$ correspond to the smaller and larger values of x and x' , respectively, $[n, m]$ are smoothness and asymptotic reciprocal power parameters, $B(a, b) = \frac{(a-1)!(b-1)!}{(a+b-1)!}$ is the β -function and ${}_2F_1(a, b; c; z)$ is Gauss' hypergeometric function.⁶⁴ The one-dimensional kernels effectively serve as a similarity function between pairs of values x and x' .

In the present work the $k^{[3,3]}$ kernel

$$k^{[3,3]}(r, r') = \frac{3}{20r_{>}^4} - \frac{6}{35} \frac{r_{<}}{r_{>}^5} + \frac{3}{56} \frac{r_{<}^2}{r_{>}^6} \quad (9)$$

was used throughout where r and r' are interatomic distances of a query structure and a reference structure, respectively. For example, the reference structure could be an equilibrium configuration, transition state structure, *etc.*. Again, the values $r_{<}$ and $r_{>}$ are the smaller and larger values of r and r' , respectively. The current approach uses the 1D kernels as local features to build a global descriptor \mathcal{D} which is then the input to the NN. Consequently, the method is referred to as KerNN = "kernels + NN" in the following.

Descriptors for H_2CO : The first, non-symmetrized variant of KerNN, KerNN^{ns}, uses the six one-dimensional kernels directly as input to the feed-forward NN with the descriptor

given by \mathcal{D}^{ns} in Equation 10. Hence, the global descriptor \mathcal{D}^{ns} takes translational and rotational invariance into account but neglects the permutational invariance of the two equivalent H-atoms.

$$\mathcal{D}^{\text{ns}} = \begin{bmatrix} k^{[3,3]}(r_{\text{CO}}, r'_{\text{CO}}) \\ k^{[3,3]}(r_{\text{CHA}}, r'_{\text{CHA}}) \\ k^{[3,3]}(r_{\text{CHB}}, r'_{\text{CHB}}) \\ k^{[3,3]}(r_{\text{OHA}}, r'_{\text{OHA}}) \\ k^{[3,3]}(r_{\text{OHB}}, r'_{\text{OHB}}) \\ k^{[3,3]}(r_{\text{HAHB}}, r'_{\text{HAHB}}) \end{bmatrix} \quad \mathcal{D}^{\text{s}} = \begin{bmatrix} k^{[3,3]}(r_{\text{CO}}, r'_{\text{CO}}) \\ k^{[3,3]}(r_{\text{CHA}}, r'_{\text{CHA}}) + k^{[3,3]}(r_{\text{CHB}}, r'_{\text{CHB}}) \\ k^{[3,3]}(r_{\text{OHA}}, r'_{\text{OHA}}) + k^{[3,3]}(r_{\text{OHB}}, r'_{\text{OHB}}) \\ k^{[3,3]}(r_{\text{CHA}}, r'_{\text{CHA}})^2 + k^{[3,3]}(r_{\text{CHB}}, r'_{\text{CHB}})^2 \\ k^{[3,3]}(r_{\text{OHA}}, r'_{\text{OHA}})^2 + k^{[3,3]}(r_{\text{OHB}}, r'_{\text{OHB}})^2 \\ k^{[3,3]}(r_{\text{HAHB}}, r'_{\text{HAHB}}) \end{bmatrix} \quad (10)$$

The second variant of KerNN, KerNN^s, accounts for permutational invariance of equivalent H-atoms explicitly. The approach chosen to include permutation invariance into KerNN is inspired by Reference 59, which uses fundamental invariants.¹⁰ In contrast to the primary and secondary polynomials in PIPs⁶⁰ and the polynomials in the PIP-NN method,⁵⁸ fundamental invariants comprise the minimum number of invariants necessary to generate all invariant polynomials. Dedicated software to calculate the fundamental invariants using King’s algorithm exist^{68,69} and exemplary fundamental invariants for a selection of molecules can be found in Reference 59. The permutationally invariant descriptor \mathcal{D}^{s} used here is given explicitly in Equation 10. The interatomic distances of the optimized structure serve as reference r'_i .

Descriptors for $[\text{HeH}_2]^+$: The PES for HeH_2^+ is also represented by two different global descriptors. The first, \mathcal{D}^{ns} , does not take the permutational invariance into account, while the second, \mathcal{D}^{s} includes it using fundamental invariants, see Equation 11. The reference structures r'_i for \mathcal{D}^{ns} and \mathcal{D}^{s} differed: for \mathcal{D}^{ns} it was the linear $\text{H}_\text{A}\text{-H}_\text{B}\text{-He}$ arrangement with

$r'_{\text{H}_A\text{He}} = 2.121$ and $r'_{\text{H}_B\text{He}} = 1.021$ Å whereas for \mathcal{D}^s a symmetrized structure is required which was chosen to be the linear H-He-H arrangement with $r'_{\text{H-He}} = 0.9$ Å were used. One advantage of using the one-dimensional kernel descriptors for systems in which the full dissociation of the molecule is conceivable is that they go to zero for large r (see Figure S1).

$$\mathcal{D}^{\text{ns}} = \begin{bmatrix} k^{[3,3]}(r_{\text{H}_A\text{He}}, r'_{\text{H}_A\text{He}}) \\ k^{[3,3]}(r_{\text{H}_B\text{He}}, r'_{\text{H}_B\text{He}}) \\ k^{[3,3]}(r_{\text{H}_A\text{H}_B}, r'_{\text{H}_A\text{H}_B}) \end{bmatrix} \quad \mathcal{D}^s = \begin{bmatrix} k^{[3,3]}(r_{\text{H}_A\text{He}}, r'_{\text{H}_A\text{He}}) + k^{[3,3]}(r_{\text{H}_B\text{He}}, r'_{\text{H}_B\text{He}}) \\ k^{[3,3]}(r_{\text{H}_A\text{He}}, r'_{\text{H}_A\text{He}})^2 + k^{[3,3]}(r_{\text{H}_B\text{He}}, r'_{\text{H}_B\text{He}})^2 \\ k^{[3,3]}(r_{\text{H}_A\text{H}_B}, r'_{\text{H}_A\text{H}_B}) \end{bmatrix} \quad (11)$$

Descriptors for hydrogen oxalate: For hydrogen oxalate, only a non permutationally invariant descriptor was employed. It is constructed from 21 one-dimensional $k^{[3,3]}$ kernels, one for each interatomic distance. The optimized hydrogen oxalate structure served as reference structure.

Data Availability

The codes and data for the present study are available from <https://github.com/MMunibas/KerNN> upon publication.

Acknowledgment

The authors gratefully acknowledge financial support from the Swiss National Science Foundation through grants 200020_219779 (MM), 200021_215088 (MM), the NCCR-MUST (MM), the AFOSR (MM), and the University of Basel (MM).

Competing Interests

The authors declare no competing interests.

Supporting Information: The Bigger the Better? Accurate Molecular Potential Energy Surfaces from Minimalist Neural Networks

Methods

Table S1: Parameters and hyperparameters of the neural networks used throughout this work.

	H ₂ CO		HeH ₂ ⁺		H. Oxa.
	KerNN ^{ns}	KerNN ^s	KerNN ^{ns}	KerNN ^s	KerNN ^{ns}
$N_{\text{in}}^{\text{nodes}}$	6	7	3	3	21
$N_{\text{hidden}}^{\text{nodes}}$	20	20	40	40	50
$N_{\text{hidden}}^{\text{layers}}$	2	2	2	2	2
ω_F	10	10	1	1	10
ω_μ	5	–	–	–	5
ω_Q	2	–	–	–	2
N_{params}	1001	1021	3481	3481	6608

Table S2: Grid for the triatomic HeH₂⁺ potential. All values are given in Å and degrees, respectively. The quantities are given as min/max/step.

Quantity / Diatom	H ₂ ⁺	HeH ⁺
r	0.5/5/0.2 and 6/50/1	0.5/5/0.2
R	0.5/5/0.2 and 6/50/1	0.5/5/0.2
Θ	0/180/15	0/180/15
N_{tot}	58357	6877

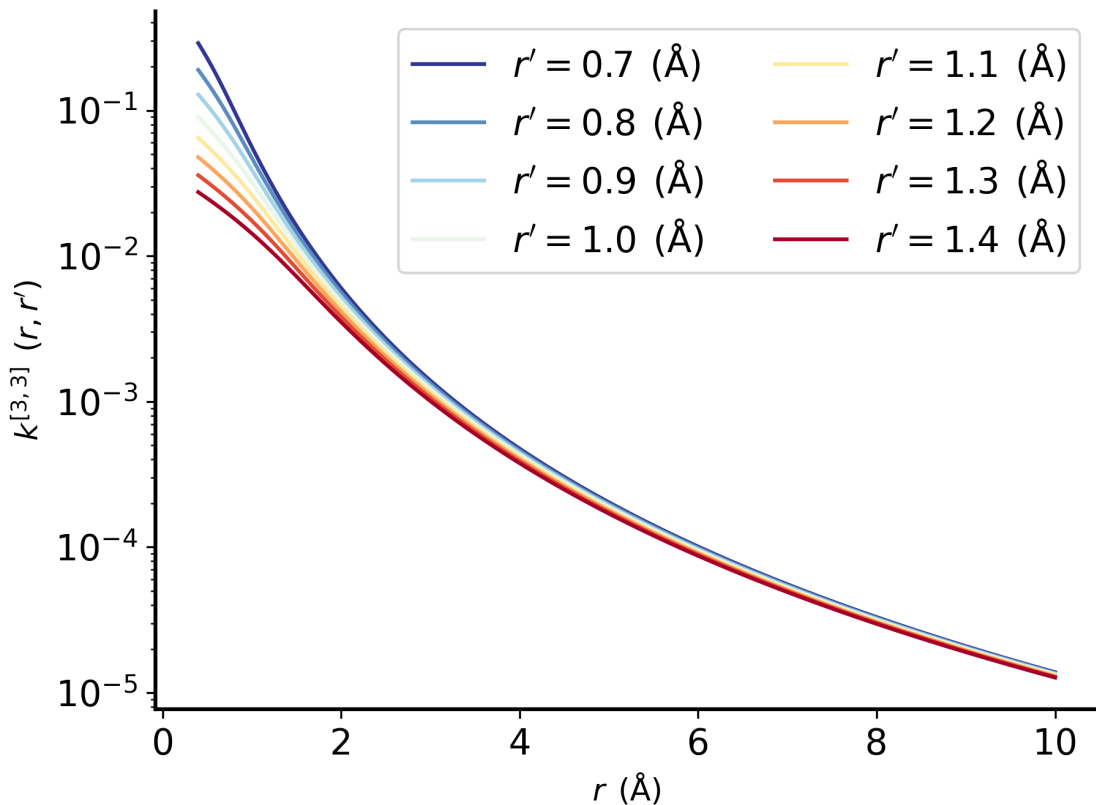


Figure S1: The one-dimensional $k^{[3,3]}(r, r')$ kernel as a function of r and for different reference values r' . The curves illustrate the asymptotic behaviour of the curves. Note that the y-axis is displayed on a logarithmic scale.

Bound state calculations for HeH_2^+

Ro-vibrational bound states have been calculated for different J (total angular momentum) states with e and f symmetries for both *ortho*- and *para*- HeH_2^+ complex. The DVR3D program²⁹ was used to solve the eigenvalue problem. Jacobian coordinates were chosen to represent the spectroscopic system in a 3D discrete variable representation (DVR) formulation. The radial grids along the R and r coordinates were defined by 86 and 32 Gauss-Laguerre quadrature points, respectively and for the angular grid (Jacobi angle θ) 36 Gauss-Legendre points were used. The wavefunctions along R and r were constructed using Morse oscillator functions while the angular part of the wavefunctions was represented by Legendre polynomials. For the r -degree of freedom (H_2^+), $r_e = 2.5 a_0$, $D_e = 0.1026 E_h$ and $\omega_e = 0.018 E_h$

were used whereas for R the values were $R_e = 11.5 a_0$, $D_e = 0.08 E_h$, and $\omega_e = 0.00065 E_h$. These parameters were chosen so that a large region in the configuration space can be covered by the wavefunction to obtain the near dissociation states. The r_2 -embedding²⁹ was used to compute the $J > 0$ states, where the z -axis is parallel to R in body-fixed Jacobi coordinates. In the r_2 -embedding, calculations with $ipar = 1$ and 0 correspond to the *ortho*- and *para*- H_2^+ states, respectively, while the e and f symmetries are defined by the parity operator p . Coriolis couplings were included in the Hamiltonian for $J > 0$ calculations.

Results and discussion

H_2CO

Table S3: Harmonic frequencies as obtained on the KerNN^{ns} and KerNN^s PESs for H_2CO in comparison to their CCSD(T)-F12B/aug-cc-pVTZ-F12 reference frequencies. These are compared to three PESs for H_2CO based on the RKHS+F¹⁷ method, PhysNet¹⁶ and obtained from kernel ridge regression using the FCHL descriptor,¹⁸ which were reported in Reference.¹² All PESs have been trained on the same reference data set containing a total of 4001 H_2CO structures with corresponding energies and forces.

(cm^{-1})	KerNN ^{ns}	KerNN ^s	RKHS+F	PhysNet	FCHL	CCSD(T)-F12
1	1186.4	1186.5	1186.4	1186.4	1186.5	1186.5
2	1267.7	1267.9	1268.1	1268.2	1268.0	1268.2
3	1532.5	1532.6	1532.6	1532.6	1532.7	1532.7
4	1776.4	1776.5	1776.4	1776.4	1776.4	1776.4
5	2933.4	2933.8	2933.5	2933.6	2933.6	2933.8
6	3006.0	3005.6	3005.8	3005.7	3005.6	3005.8
MAE	0.2	0.1	0.1	0.1	0.1	

Table S4: Test set errors for KerNN^{ns} trained on energies, forces and dipole moments using the loss function given in Equation 7. Errors of the energy, forces and dipole moments are given in kcal/mol, kcal/mol/Å/ and Debye, respectively.

KerNN ^{ns}	
MAE(E):	0.00052
RMSE(E):	0.00090
MAE(F):	0.00902
RMSE(F):	0.01786
MAE(D):	0.00071
RMSE(D):	0.00129

Table S5: Computational timings for KerNN^{ns}, KerNN^s, RKHS+F, PhysNet and kernel ridge regression with the FCHL descriptor. The reported values correspond to (consecutive) energy and force evaluations as would be required in a MD simulation. Numbers in plain (boldface) letters correspond to Python implementations used via ASE (FORTRAN implementations used via CHARMM).* Pure FORTRAN

(ms)	KerNN ^{ns}	KerNN ^s	RKHS+F	PhysNet	FCHL
time/eval	1.3/ 0.012/0.003 *	2.0	0.3	34	92

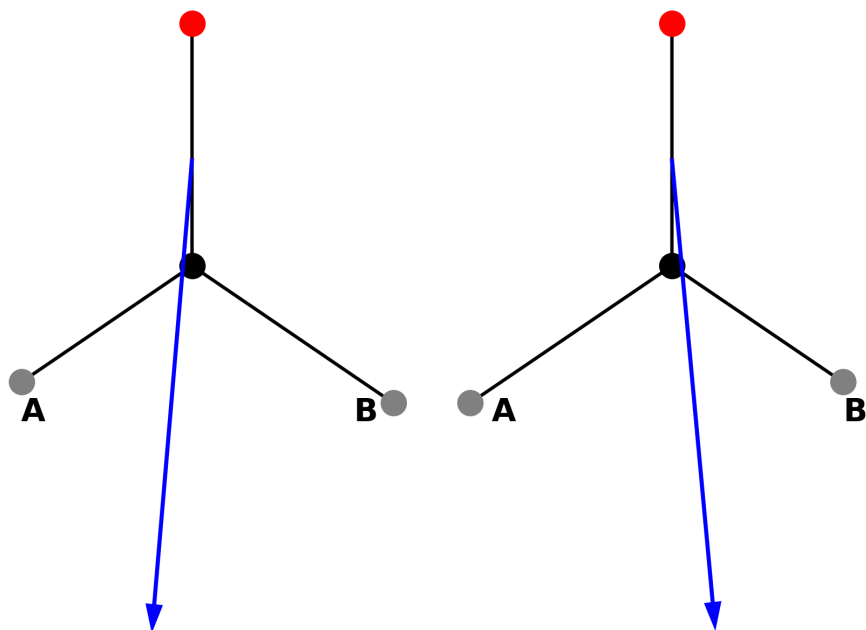


Figure S2: Two symmetric H₂CO configurations in which two sets of C-H bond lengths are the same (the C-H_A bond length in the left is the same as C-H_B in the right configuration). In the permutationally invariant formulation, KerNN^s, the two configurations are described by the same molecular descriptor \mathcal{D}^s which leads to the same potential energy by construction. Since in the given formulation, the dipole moment (blue) is obtained from $\sum_{\alpha=1}^3 \sum_{i=1}^N q_i x_{i,\alpha}$ this would require different partial charges for, *e.g.*, H_A (left) and H_A (right). As the two structures have the same descriptor and the formulation, therefore, lacks a direct mapping to the partial charges (*i.e.* in this case we would try to predict two sets of partial charges with the same descriptor), it is not possible to learn the dipole moment with KerNN^s.

HeH₂⁺

Table S6: Harmonic frequencies as obtained on the KerNN^{ns} PES for a linear H-H-He arrangement in comparison to their UCCSD(T)/aug-cc-pV5Z reference frequencies.

(cm ⁻¹)	KerNN ^{ns}	CCSD(T)
1	711.5	717.9
2	711.5	717.9
3	989.2	986.6
4	1959.1	1935.4

Table S7: Bound energy levels from DVR3D calculations for e- and f-parity, *ortho* (o) and *para* (p) He-H₂⁺ for $J = 0$ and $J = 1$ in cm⁻¹. The results from the KerNN^{ns} PES trained on UCCSD(T)/aug-cc-pV5Z level of theory data are compared to theoretical results derived from a FCI/aug-cc-pV5Z PES.³⁰

o/p	J	parity	n	FCI/DVR3D	KerNN ^{ns} /DVR3D
o	0	e	1	-1793.7632	-1793.3578
o	0	e	2	-1062.6727	-1064.2547
o	0	e	3	-657.6932	-658.5876
o	0	e	4	-538.1281	-541.3037
o	0	e	5	-254.3251	-257.9835
o	0	e	6	-190.0415	-193.8107
o	0	e	7	-48.5279	-54.2574
o	0	e	8	19.0868	15.2201
o	0	e	9	40.0360	35.9073
o	0	e	10	55.8602	50.0858
o	1	e	1	-1785.5973	-1783.5868
o	1	e	2	-1153.7813	-1152.7036
o	1	e	3	-1055.3035	-1055.2840
o	1	e	4	-650.0284	-649.3253

o	1	e	5	-564.6730	-565.8948
o	1	e	6	-531.0451	-532.6107
o	1	e	7	-263.2100	-264.2067
o	1	e	8	-248.8408	-250.9070
o	1	e	9	-186.1513	-188.1117
o	1	e	10	-174.2152	-175.6023
o	1	e	11	-68.9712	-71.8441
o	1	e	12	-45.1411	-49.2928
o	1	e	13	-27.0299	-29.0847
o	1	e	14	22.8241	20.0109
o	1	e	15	30.5164	26.4763
o	1	e	16	43.4379	40.8763
o	1	e	17	54.5753	50.1988
o	1	e	18	57.2317	52.8676
o	1	f	1	-1153.4648	-1152.3852
o	1	f	2	-563.7240	-564.9356
o	1	f	3	-262.8397	-263.8038
o	1	f	4	-175.8616	-177.0772
o	1	f	5	-68.7581	-71.6364
o	1	f	6	-27.5094	-29.5545
o	1	f	7	29.9118	25.7797
o	1	f	8	54.6476	50.1420
<hr/>					
p	0	e	1	-1793.7639	-1793.3585
p	0	e	2	-1062.7083	-1064.2907
p	0	e	3	-659.6723	-660.5809
p	0	e	4	-538.8389	-542.0167
p	0	e	5	-300.6517	-303.4586

p	0	e	6	-214.3129	-218.8744
p	0	e	7	-109.8684	-114.4646
p	0	e	8	-60.7249	-65.7386
p	0	e	9	-16.0670	-21.9619
p	0	e	10	-1.1504	-7.3349
<hr/>					
p	1	e	1	-1785.5980	-1783.5875
p	1	e	2	-1153.7480	-1152.6700
p	1	e	3	-1055.3364	-1055.3174
p	1	e	4	-651.8816	-651.1921
p	1	e	5	-562.5239	-563.7546
p	1	e	6	-531.5656	-533.1320
p	1	e	7	-295.1356	-296.3543
p	1	e	8	-212.6546	-213.8757
p	1	e	9	-209.9754	-212.8800
p	1	e	10	-154.5125	-155.3351
p	1	e	11	-105.5427	-108.6013
p	1	e	12	-57.0589	-60.4399
p	1	e	13	-14.3679	-18.6642
p	1	e	14	-0.4477	-5.0399
p	1	f	1	-1153.4283	-1152.3484
p	1	f	2	-561.2379	-562.4576
p	1	f	3	-212.4739	-213.6612
p	1	f	4	-154.6979	-155.4914

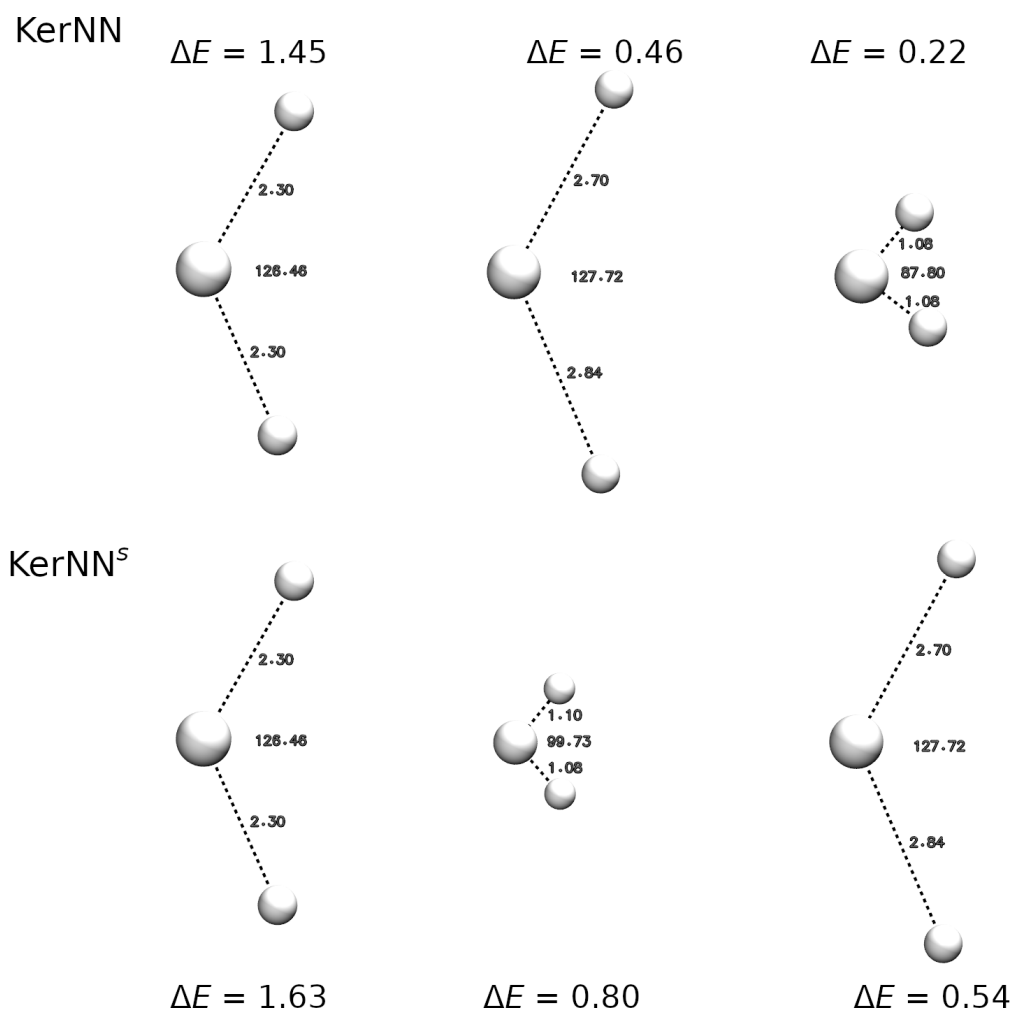


Figure S3: Test set structures with the highest prediction error as compared to direct UCCSD(T) *ab initio* calculations for both KerNN^{ns} and KerNN^s. For each structure the associated bond length (in Å), the H-He-H angle (in °) and the absolute energy difference between reference and predicted energy (in kcal/mol) are shown. Two out of three outliers are the same in KerNN^{ns} and KerNN^s.

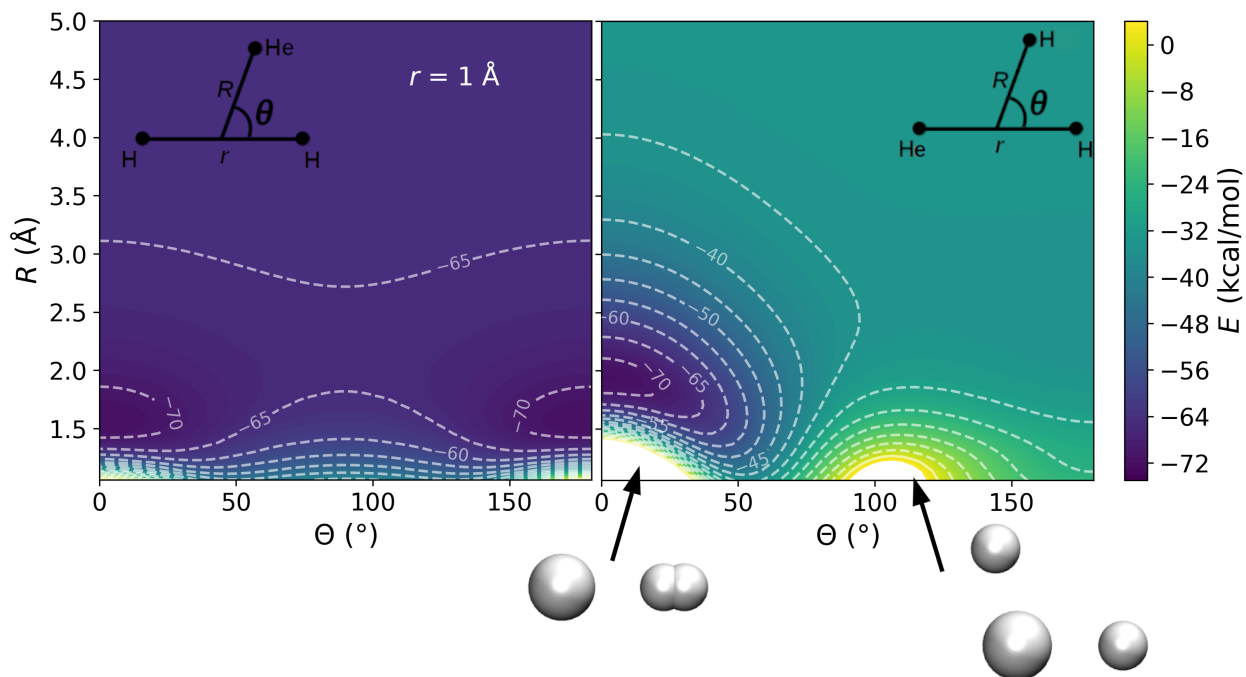


Figure S4: Two-dimensional cuts through the 3D KerNN^{ns} PES for He + H₂⁺ (left) and HeH⁺ + H (right) channels. The separation of the diatomics, H₂⁺ and HeH⁺ is fixed at ~ 1 Å. Repulsive regions are illustrated with a schematic and energies that exceed 5 kcal/mol are shown in white.

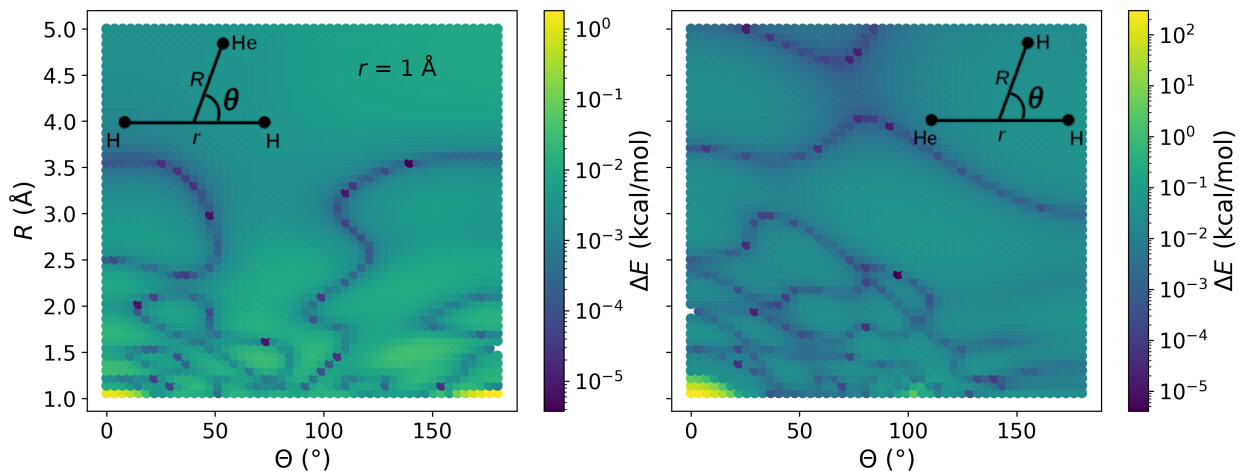


Figure S5: Absolute errors of the KerNN^{ns} PES for He + H₂⁺ (left) and HeH⁺ + H (right) channels with respect to CCSD(T)/aug-cc-pV5Z reference energies for 2500 grid points. The largest differences are found in the repulsive regions. The predictions yield MAE(E) of 0.05 and 0.70 kcal/mol for the He + H₂⁺ and HeH⁺ + H channels, respectively. Excluding the ten predictions with largest error for the latter (residing exclusively in the repulsive region) yields a MAE(E) of 0.06 kcal/mol.

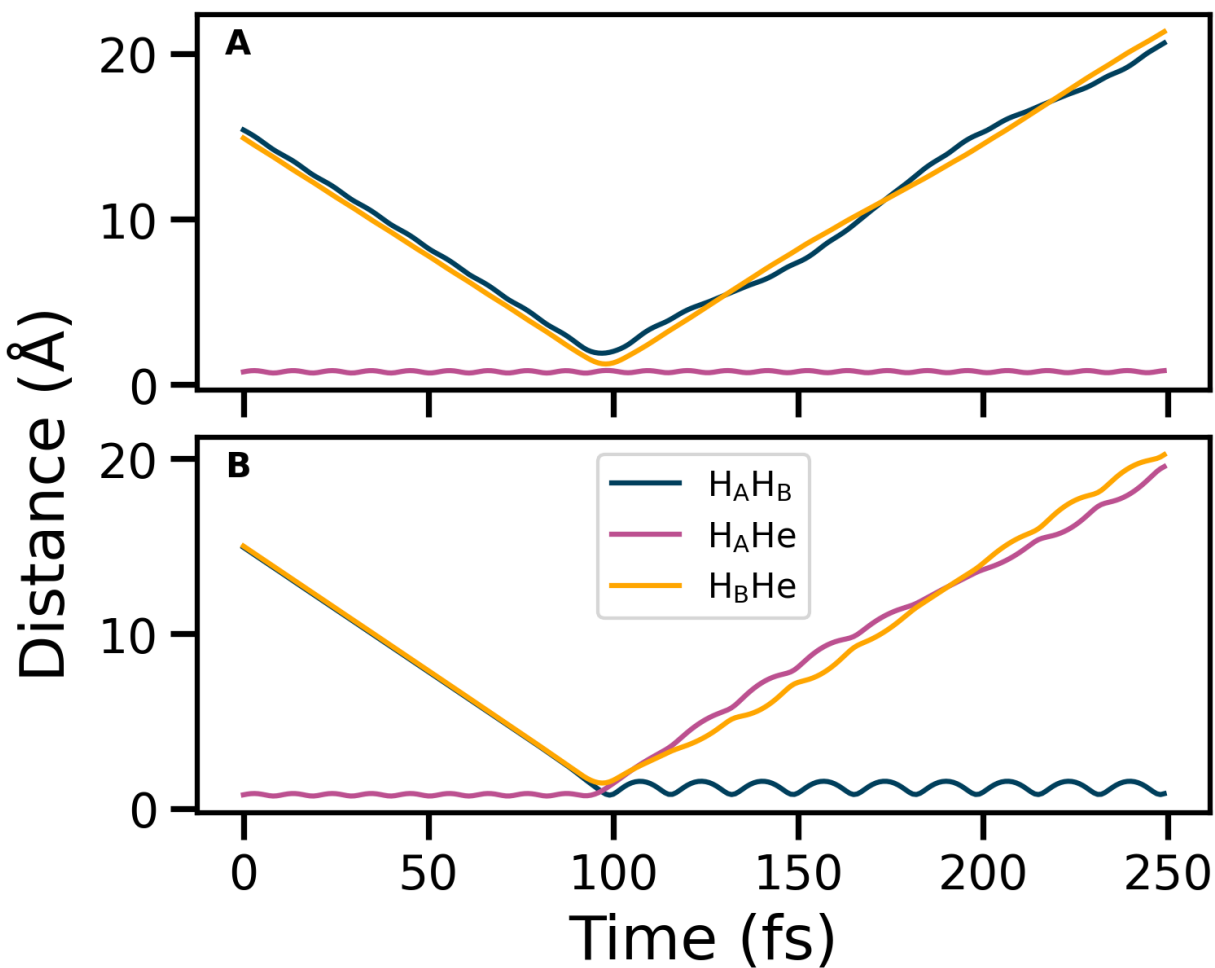


Figure S6: Exemplary non-reactive (A) and reactive (B) collision trajectories obtained from KerNN^{ns}. Initially, H_AHe forms the bonded diatom with a vibrational energy that has been assigned by drawing random momenta from a Maxwell-Boltzmann distribution corresponding to 300 K (translation and rotation have been projected out). H_B , initially placed at a distance of 15 Å from the CoM of the diatom, is accelerated towards the CoM of the diatom with a kinetic energy corresponding to ~ 1 eV.

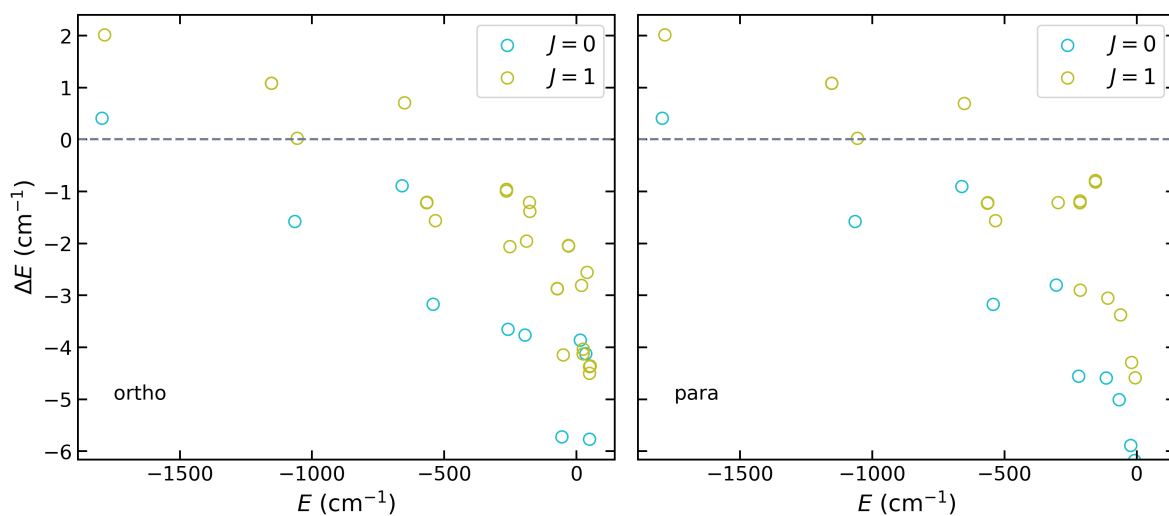


Figure S7: Comparison of the bound energy levels from DVR3D calculations for $J = 0$ and 1, e - and f - parity, and *ortho*- and *para*- HeH_2^+ as determined on the KerNN^{ns}(UCCSD(T)) and a RKHS(FCI) PES.³⁰ $\Delta E = E_{\text{KerNN}} - E_{\text{RKHS}}$ and illustrates that KerNN^{ns} trained on UCCSD(T) typically underestimates the bound state energy in comparison to the FCI PES, in particular in the near-dissociative region.

Hydrogen Oxalate

Table S8: Averaged test set errors for the **KerNN^{ns}** and **PhysNet PES** trained on the MP2/aug-cc-pVTZ level data set. Energy, force and dipole moment errors are given in kcal/mol, kcal/mol/Å, and Debye, respectively.

	MAE(E)	RMSE(E)	MAE(F)	RMSE(F)	MAE(μ)	RMSE(μ)
KerNN^{ns}	0.013	0.033	0.089	0.187	0.0014	0.0027
PhysNet	0.009	0.047	0.065	0.459	0.0018	0.0054

References

- (1) Van Gunsteren, W. F.; Berendsen, H. J. Computer simulation of molecular dynamics: methodology, applications, and perspectives in chemistry. *Angew. Chem., Int. Ed. Engl.* **1990**, *29*, 992–1023.
- (2) Karplus, M.; Petsko, G. A. Molecular dynamics simulations in biology. *Nature* **1990**, *347*, 631–639.
- (3) Durrant, J. D.; McCammon, J. A. Molecular dynamics simulations and drug discovery. *BMC Biology* **2011**, *9*, 1–9.
- (4) Vanommeslaeghe, K.; Hatcher, E.; Acharya, C.; Kundu, S.; Zhong, S.; Shim, J.; Darian, E.; Guvench, O.; Lopes, P.; Vorobyov, I. et al. CHARMM general force field: A force field for drug-like molecules compatible with the CHARMM all-atom additive biological force fields. *J. Comput. Chem.* **2010**, *31*, 671–690.
- (5) Hwang, W.; Austin, S. L.; Blondel, A.; Boittier, E. D.; Boresch, S.; Buck, M.; Buckner, J.; Caffisch, A.; Chang, H.-T.; Cheng, X. et al. CHARMM at 45: Enhancements in accessibility, functionality, and speed. *J. Phys. Chem. B* **2024**, *128*, 9976–10042.
- (6) Unke, O. T.; Chmiela, S.; Sauceda, H. E.; Gastegger, M.; Poltavsky, I.; Schütt, K. T.; Tkatchenko, A.; Müller, K.-R. Machine learning force fields. *Chem. Rev.* **2021**, *121*, 10142–10186.
- (7) Käser, S.; Vazquez-Salazar, L. I.; Meuwly, M.; Töpfer, K. Neural network potentials for chemistry: concepts, applications and prospects. *Digital Discovery* **2023**, *2*, 28–58.
- (8) Qu, C.; Yu, Q.; Van Hoozen Jr, B. L.; Bowman, J. M.; Vargas-Hernández, R. A. Assessing Gaussian process regression and permutationally invariant polynomial approaches to represent high-dimensional potential energy surfaces. *J. Chem. Theory Comput.* **2018**, *14*, 3381–3396.

- (9) Wang, Y.; Takaba, K.; Chen, M. S.; Wieder, M.; Xu, Y.; Zhu, T.; Zhang, J. Z. H.; Nagle, A.; Yu, K.; Wang, X. et al. On the design space between molecular mechanics and machine learning force fields. *arXiv e-prints* **2024**, arXiv:2409.01931.
- (10) Derksen, H.; Kemper, G. *Computational invariant theory*; Springer, 2015.
- (11) Baydin, A. G.; Pearlmutter, B. A.; Radul, A. A.; Siskind, J. M. Automatic differentiation in machine learning: a survey. *J. Mach. Learn. Res.* **2017**, *18*, 5595–5637.
- (12) Käser, S.; Koner, D.; Christensen, A. S.; von Lilienfeld, O. A.; Meuwly, M. Machine Learning Models of Vibrating H₂CO: Comparing Reproducing Kernels, FCHL, and PhysNet. *J. Phys. Chem. A* **2020**, *124*, 8853–8865.
- (13) Müller, K.-R.; Finke, M.; Murata, N.; Schulten, K.; Amari, S.-I. A numerical study on learning curves in stochastic multilayer feedforward networks. *Neural Comput.* **1996**, *8*, 1085–1106.
- (14) Huang, B.; Von Lilienfeld, O. A. Communication: Understanding molecular representations in machine learning: The role of uniqueness and target similarity. *J. Chem. Phys.* **2016**, *145*, 161102.
- (15) Christensen, A. S.; Von Lilienfeld, O. A. On the role of gradients for machine learning of molecular energies and forces. *Mach. Learn.: Sci. Technol.* **2020**, *1*, 045018.
- (16) Unke, O. T.; Meuwly, M. PhysNet: A neural network for predicting energies, forces, dipole moments, and partial charges. *J. Chem. Theory Comput.* **2019**, *15*, 3678–3693.
- (17) Koner, D.; Meuwly, M. Permutationally invariant, reproducing kernel-based potential energy surfaces for polyatomic molecules: From formaldehyde to acetone. *J. Chem. Theory Comput.* **2020**, *16*, 5474–5484.
- (18) Faber, F. A.; Christensen, A. S.; Huang, B.; Von Lilienfeld, O. A. Alchemical and

- structural distribution based representation for universal quantum machine learning. *J. Chem. Phys.* **2018**, *148*, 241717.
- (19) Poltavsky, I.; Charkin-Gorbulin, A.; Puleva, M.; Cordeiro Fonseca, G.; Batatia, I.; Browning, N. J.; Chmiela, S.; Cui, M.; Frank, J. T.; Heinen, S. et al. Crash Testing Machine Learning Force Fields for Molecules, Materials, and Interfaces: Model Analysis in the TEA Challenge 2023. *ChemRxiv* <https://doi.org/10.26434/chemrxiv-2024-ctdm3> **2024**,
- (20) Poltavsky, I.; Puleva, M.; Charkin-Gorbulin, A.; Cordeiro Fonseca, G.; Batatia, I.; Browning, N. J.; Chmiela, S.; Cui, M.; Frank, J. T.; Heinen, S. et al. Crash Testing Machine Learning Force Fields for Molecules, Materials, and Interfaces: Molecular Dynamics in the TEA Challenge 2023. *ChemRxiv* <https://doi.org/10.26434/chemrxiv-2024-jhm5l> **2024**,
- (21) Chuang, M.-C.; Foltz, M. F.; Moore, C. B. T_1 barrier height, $S_1 - -T_1$ intersystem crossing rate, and S_0 radical dissociation threshold for H_2CO , D_2CO , and $HDCO$. *J. Chem. Phys.* **1987**, *87*, 3855–3864.
- (22) Dawes, R.; Ndengué, S. A. Single- and multireference electronic structure calculations for constructing potential energy surfaces. *Intern. Rev. Phys. Chem.* **2016**, *35*, 441–478.
- (23) Herndon, S. C.; Nelson Jr, D. D.; Li, Y.; Zahniser, M. S. Determination of line strengths for selected transitions in the v_2 band relative to the v_1 and v_5 bands of H_2CO . *J. Quant. Spectrosc. Radiat. Transf.* **2005**, *90*, 207–216.
- (24) Töpfer, K.; Koner, D.; Erramilli, S.; Ziegler, L. D.; Meuwly, M. Molecular-level understanding of the rovibrational spectra of N_2O in gaseous, supercritical, and liquid SF_6 and Xe . *J. Chem. Phys.* **2023**, *158*, 144302.
- (25) Kumar, P.; Marx, D. Quantum corrections to classical time-correlation functions: Hydrogen bonding and anharmonic floppy modes. *J. Chem. Phys.* **2004**, *121*, 9.

- (26) Larsen, A. H.; Mortensen, J. J.; Blomqvist, J.; Castelli, I. E.; Christensen, R.; Dułak, M.; Friis, J.; Groves, M. N.; Hammer, B.; Hargus, C. et al. The atomic simulation environment – a Python library for working with atoms. *J. Phys. Condens. Matter* **2017**, *29*, 273002.
- (27) Bouilloud, M.; Fray, N.; Bénilan, Y.; Cottin, H.; Gazeau, M.-C.; Jolly, A. Bibliographic review and new measurements of the infrared band strengths of pure molecules at 25 K: H₂O, CO₂, CO, CH₄, NH₃, CH₃OH, HCOOH and H₂CO. *Mon. Not. R. Astron. Soc.* **2015**, *451*, 2145–2160.
- (28) Unke, O. T.; Meuwly, M. Toolkit for the construction of reproducing kernel-based representations of data: Application to multidimensional potential energy surfaces. *J. Chem. Inf. and Mod.* **2017**, *57*, 1923–1931.
- (29) Tennyson, J.; Kostin, M. A.; Barletta, P.; Harris, G. J.; Polyansky, O. L.; Ramanlal, J.; Zobov, N. F. DVR3D: a program suite for the calculation of rotation–vibration spectra of triatomic molecules. *Comput. Phys. Commun.* **2004**, *163*, 85–116.
- (30) Koner, D.; Veliz, J. C. S. V.; van der Avoird, A.; Meuwly, M. Near dissociation states for H₂⁺–He on MRCI and FCI potential energy surfaces. *Phys. Chem. Chem. Phys.* **2019**, *21*, 24976–24983.
- (31) Asvany, O.; Schlemmer, S.; van der Avoird, A.; Szidarovszky, T.; Császár, A. G. Vibrational spectroscopy of H₂He⁺ and D₂He⁺. *J. Mol. Spectrosc.* **2021**, *377*, 111423.
- (32) Margulis, B.; Horn, K. P.; Reich, D. M.; Upadhyay, M.; Kahn, N.; Christianen, A.; van der Avoird, A.; Groenenboom, G. C.; Meuwly, M.; Koch, C. P. et al. Tomography of Feshbach resonance states. *Science* **2023**, *380*, 77–81.
- (33) Horn, K. P.; Vazquez-Salazar, L. I.; Koch, C. P.; Meuwly, M. Improving potential energy surfaces using measured Feshbach resonance states. *Sci. Adv.* **2024**, *10*, eadi6462.

- (34) Horn, K. P.; Upadhyay, M.; Margulis, B.; Reich, D. M.; Narevicius, E.; Meuwly, M.; Koch, C. P. Feshbach resonances in cold collisions as a benchmark for state of the art ab initio theory. *arXiv preprint arXiv:2408.13197* **2024**,
- (35) Wolke, C. T.; DeBlase, A. F.; Leavitt, C. M.; McCoy, A. B.; Johnson, M. A. Diffuse vibrational signature of a single proton embedded in the oxalate scaffold, $\text{HO}_2\text{CCO}_2^-$. *J. Phys. Chem. A* **2015**, *119*, 13018–13024.
- (36) Xu, Z.-H.; Meuwly, M. Vibrational spectroscopy and proton transfer dynamics in protonated oxalate. *J. Phys. Chem. A* **2017**, *121*, 5389–5398.
- (37) Käser, S.; Unke, O. T.; Meuwly, M. Reactive dynamics and spectroscopy of hydrogen transfer from neural network-based reactive potential energy surfaces. *New J. Phys.* **2020**, *22*, 055002.
- (38) Blumer, A.; Ehrenfeucht, A.; Haussler, D.; Warmuth, M. K. Occam’s razor. *Inf. Process. Lett.* **1987**, *24*, 377–380.
- (39) Domingos, P. The role of Occam’s razor in knowledge discovery. *Data Min. Knowl. Discov.* **1999**, *3*, 409–425.
- (40) Abdin, M.; Aneja, J.; Awadalla, H.; Awadallah, A.; Awan, A. A.; Bach, N.; Bahree, A.; Bakhtiari, A.; Bao, J.; Behl, H. et al. Phi-3 Technical Report: A Highly Capable Language Model Locally on Your Phone. *arXiv e-prints* **2024**, arXiv:2404.14219.
- (41) Tan, M.; Le, Q. V. EfficientNet: Rethinking Model Scaling for Convolutional Neural Networks. *arXiv e-prints* **2019**, arXiv:1905.11946.
- (42) Langer, M. F.; Pozdnyakov, S. N.; Ceriotti, M. Probing the effects of broken symmetries in machine learning. *arXiv e-prints* **2024**, arXiv:2406.17747.
- (43) Koner, D.; San Vicente Veliz, J. C.; Bemish, R. J.; Meuwly, M. Accurate reproducing kernel-based potential energy surfaces for the triplet ground states of N_2O and dynamics

- for the $\text{N} + \text{NO} \leftrightarrow \text{O} + \text{N}_2$ and $\text{N}_2 + \text{O} \rightarrow 2\text{N} + \text{O}$ reactions. *Phys. Chem. Chem. Phys.* **2020**, *22*, 18488–18498.
- (44) Koner, D.; Bemish, R. J.; Meuwly, M. The $\text{C}(^3\text{P}) + \text{NO}(X^2\Pi) \rightarrow \text{O}(^3\text{P}) + \text{CN}(X^2\Sigma^+)$, $\text{N}(^2\text{D})/\text{N}(^4\text{S}) + \text{CO}(X^1\Sigma^+)$ reaction: Rates, branching ratios, and final states from 15 K to 20 000 K. *J. Chem. Phys.* **2018**, *149*, 094305.
- (45) Smith, J. S.; Isayev, O.; Roitberg, A. E. ANI-1: an extensible neural network potential with DFT accuracy at force field computational cost. *Chem. Sci.* **2017**, *8*, 3192–3203.
- (46) Werner, H.-J.; Knowles, P. J.; Knizia, G.; Manby, F. R.; Schütz, M.; Celani, P.; Gyröffy, W.; Kats, D.; Korona, T.; Lindh, R. et al. MOLPRO, version 2019, a package of ab initio programs. 2019.
- (47) Bannwarth, C.; Ehlert, S.; Grimme, S. GFN2-xTB—An accurate and broadly parametrized self-consistent tight-binding quantum chemical method with multipole electrostatics and density-dependent dispersion contributions. *J. Chem. Theory Comput.* **2019**, *15*, 1652–1671.
- (48) Kosztin, I.; Faber, B.; Schulten, K. Introduction to the diffusion Monte Carlo method. *Am. J. Phys.* **1996**, *64*, 633–644.
- (49) Käser, S.; Meuwly, M. Transfer learned potential energy surfaces: accurate anharmonic vibrational dynamics and dissociation energies for the formic acid monomer and dimer. *Phys. Chem. Chem. Phys.* **2022**, *24*, 5269–5281.
- (50) Kingma, D. P.; Ba, J. Adam: A method for stochastic optimization. *arXiv preprint arXiv:1412.6980* **2014**,
- (51) Prechelt, L. *Neural Networks: Tricks of the trade*; Springer, 2002; pp 55–69.
- (52) Raghunathan, S.; Priyakumar, U. D. Molecular representations for machine learning applications in chemistry. *Int. J. Quantum Chem.* **2022**, *122*, e26870.

- (53) Kocer, E.; Ko, T. W.; Behler, J. Neural network potentials: A concise overview of methods. *Ann. Rev. Phys. Chem.* **2022**, *73*, 163–186.
- (54) Behler, J.; Parrinello, M. Generalized neural-network representation of high-dimensional potential-energy surfaces. *Phys. Rev. Lett.* **2007**, *98*, 146401.
- (55) Zou, S.; Bowman, J. M. A new ab initio potential energy surface describing acetylene/vinylidene isomerization. *Chem. Phys. Lett.* **2003**, *368*, 421–424.
- (56) Prudente, F. V.; Acioli, P. H.; Neto, J. S. The fitting of potential energy surfaces using neural networks: Application to the study of vibrational levels of H³⁺. *J. Chem. Phys.* **1998**, *109*, 8801–8808.
- (57) Nguyen, H. T.; Le, H. M. Modified feed-forward neural network structures and combined-function-derivative approximations incorporating exchange symmetry for potential energy surface fitting. *J. Phys. Chem. A* **2012**, *116*, 4629–4638.
- (58) Jiang, B.; Guo, H. Permutation invariant polynomial neural network approach to fitting potential energy surfaces. *J. Chem. Phys.* **2013**, *139*, 054112.
- (59) Shao, K.; Chen, J.; Zhao, Z.; Zhang, D. H. Communication: Fitting potential energy surfaces with fundamental invariant neural network. *J. Chem. Phys.* **2016**, *145*, 071101.
- (60) Braams, B. J.; Bowman, J. M. Permutationally invariant potential energy surfaces in high dimensionality. *Int. Rev. Phys. Chem.* **2009**, *28*, 577–606.
- (61) Xie, Z.; Bowman, J. M. Permutationally invariant polynomial basis for molecular energy surface fitting via monomial symmetrization. *J. Chem. Theory Comput.* **2010**, *6*, 26–34.
- (62) Bowman, J. M.; Czako, G.; Fu, B. High-dimensional ab initio potential energy surfaces for reaction dynamics calculations. *Phys. Chem. Chem. Phys.* **2011**, *13*, 8094–8111.
- (63) Aronszajn, N. Theory of reproducing kernels. *Trans. Am. Math. Soc.* **1950**, *68*, 337–404.

- (64) Ho, T.-S.; Rabitz, H. A general method for constructing multidimensional molecular potential energy surfaces from ab initio calculations. *J. Chem. Phys.* **1996**, *104*, 2584.
- (65) San Vicente Veliz, J. C.; Koner, D.; Schwilk, M.; Bemish, R. J.; Meuwly, M. The $N(^4S) + O_2(X^3\Sigma_g^-) \leftrightarrow O(^3P) + NO(X^2\Pi)$ Reaction: Thermal and Vibrational Relaxation Rates for the $^2A'$, $^4A'$ and $^2A''$ States. *Phys. Chem. Chem. Phys.* **2020**, *22*, 3927–3939.
- (66) Pezzella, M.; Koner, D.; Meuwly, M. Formation and Stabilization of Ground and Excited-State Singlet O_2 upon Recombination of 3P Oxygen on Amorphous Solid Water. *J. Phys. Chem. Lett.* **2020**, *11*, 2171–2176.
- (67) Soldán, P.; Hutson, J. M. On the long-range and short-range behavior of potentials from reproducing kernel Hilbert space interpolation. *J. Chem. Phys.* **2000**, *112*, 4415–4416.
- (68) King, S. A. Minimal generating sets of non-modular invariant rings of finite groups. *J. Symbolic Comput.* **2013**, *48*, 101–109.
- (69) Decker, W.; Greuel, G.-M.; Pfister, G.; Schönemann, H. SINGULAR 4-3-0 — A computer algebra system for polynomial computations. <http://www.singular.uni-kl.de>, 2022.